IN VIVO TECHNIQUES FOR DISTRACTION AND MAGNETIC RESONANCE IMAGING OF A CAUDAL INTERVERTEBRAL DISC IN A RAT-TAIL MODEL

by

Joshua James Booren

A thesis submitted to the faculty of
The University of Utah
in partial fulfillment of the requirements for the degree of

Master of Science

Department of Bioengineering

The University of Utah

August 2014

THE UNIVERSITY OF UTAH GRADUATE SCHOOL

STATEMENT OF THESIS APPROVAL

The thesis of Joshua James Booren

Has been approved by the following supervisory committee members:

Kent N. Bachus	, Chair	June 12, 2014 Date Approved
Edward Hsu	, Member	June 18, 2014 Date Approved
Julie Fritz	, Member	July 6, 2014 Date Approved

And by Patrick A. Tresco, Chair/Dean of the Department/College/School of Bioengineering and by David B. Kieda, Dean of The Graduate School.

ABSTRACT

Intervertebral discs (IVDs) are soft tissues between adjacent vertebra, which allow motion of the spine. Unfortunately, the IVD can degenerate with age, disease, and with trauma. To better understand the process of IVD degeneration and the potential for regeneration, researchers have used Ilizarov-type devices to compress and to distract the IVD using a rat-tail model. These devices transmit loads applied to two external rings surrounding the tail, to rods implanted through adjacent vertebra, either compressing or distracting the IVD. However, these devices are typically made of materials that induce artifacts with magnetic resonance imaging (MRI), the standard of human IVD assessment, and provide only gross morphology, but are inadequate to differentiate between the nucleus pulposus and the annulus fibrosus. The goal of this project was to develop an MRI-compatible Ilizarov-type device that allowed observation of nonanesthetized animals during repeated distraction treatments.

The device developed in this study was constructed of MRI-compatible polysulfone (Psf) rings and carbon fiber rods. By developing new protocols, alignment of the rings and rods were standardized and minimized vascular, neural, and muscular damage to the rat-tail. A custom feedback-controlled pneumatic system inflated a latex bladder inserted between the Psf rings. MRIs were conducted with a loop-gap single-turn solenoid seated in a bed, which

accommodated the solenoid's perpendicular orientation to the primary axis of the main magnet and maintained animal homeostasis.

In the targeted loading range of 0-10 N, the modulus of the ring/rod constructs implanted into *in vitro* rat-tails was 5±3 N/mm, but were capable of withstanding up to 32±3 N/mm. Implanting these devices into 49 anesthetized rats resulted in zero intraoperative complications. MRI images provided quantifiable separation of the nucleus pulposus and annulus fibrosus with 30 min scan times. However, two weeks after surgery, the periprosthetic tissues of 38 of the animals became inflamed, requiring treatment with antibiotics and resulted in eight deaths. While the goal of developing an MRI compatible distraction device that allowed observation of nonanesthetized animals during repeated distraction treatments was achieved, replacing the carbon-fiber rods used in this study with a more biocompatible matrix is necessary for future studies.

To my dear wife and family who've supported me and sacrificed through the educational journey.

TABLE OF CONTENTS

ACKNOWLEDGEMENTS

I appreciate the assistance of my committee, Dr. Kent Bachus, Dr. Edward Hsu, and Dr. Julie Fritz. I am grateful for MRI Specialist, Osama Abdullah, who has made substantial contributions to the project as well as the staff at the MRI Small Animal Imaging Facility at the University of Utah. Members of the University of Utah Orthopaedic Research Laboratory, Alex Drew, Andrew Guss, Dr. Heath Henninger, Christine Abraham, Saranne Ja'kel Cook, and others have offered insights, materials, and assistance to the research. Undergraduate researchers Nate Hansen and Jameson Reich volunteered many hours to assist with surgeries, imaging, and data analysis. Penny Noel and Lauren Lentsch took excellent care of animals used in the study as did the other staff at the University of Utah Comparative Medicine Center, and Beth Bowman harvested and processed the histological and immunohistochemistry specimens.

This material is based upon work supported by the National Science Foundation under Grant No. 1256065 and the Western Institute for Biomedical Research.

CHAPTER 1

INTRODUCTION

1.1. Degenerative Disc Disease

Intervertebral discs (IVDs) are the soft tissues between adjacent vertebrae in the spine, which allow the thorax to bend, to twist, and to absorb compressive loads during activities of normal daily living. As illustrated in Figure 1.1, each IVD is made up of a compression-resisting hydrated proteoglycan matrix in the center, also known as the nucleus pulposus, with a fibrous laminar ring that constrains the nucleus and withstands tensile and torsional forces between adjacent vertebrae. Type I collagen fibers obliquely form the lamellae of the annulus, providing flexibility within the structural limits of the fibers. Periodic deformation induces Type I collagen synthesis and maintains the annulus (Setton and Chen, 2004). Type II collagen and elastin fibers in the nucleus form a loose network encasing proteoglycans; the dominate proteoglycan is hydrophilic aggrecan. Hydrostatic pressure in the nucleus promotes synthesis of proteoglycans and Type II collagen (Adams and Roughley, 2006). Unfortunately, even in healthy individuals, the IVD is prone to deteriorate. By the young age of 16 years, intervertebral disc degeneration (IVDD) can begin as the vascular

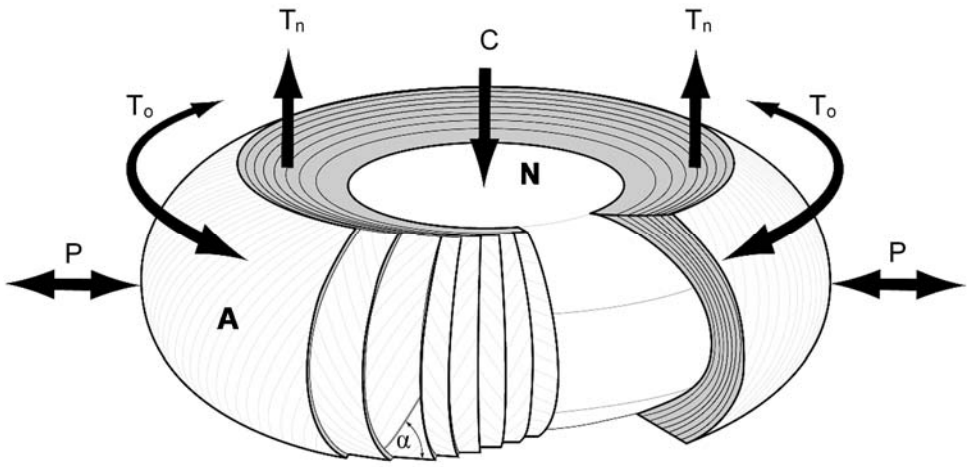

Figure 1.1: The laminar annulus pulposus rings (A) encapsulate the central nucleus pulposus (N). The nucleus withstands compressive forces (C), while the annulus withstands the resulting hydrostatic pressure (P) and resists tensile (T_n) and torsion (T_o) forces with a laminar structure of alternating fibers. The angle of the fibers (α) decreases from the outer edge of the disc inward to the nucleus with reported α = 30- 65 degrees (Adams and Roughley, 2006; Cassidy et al., 1989; Hickey and Hukins, 1980)

supply of the vertebral endplate is reduced, decreasing the resistance to compressive loads (Vo et al., 2013). With this reduction in blood flow, the predominately extracellular matrix (ECM) of the nucleus pulposus begins to decay, diminishing the cells' ability to receive nutrients and expel wastes (Bibby et al., 2005). The ability of the annulus to heal (i.e., regenerate) also decays with age and diminished vasculature. As the nucleus recedes, the annulus disorganizes, then fractures and collapses into the nuclear space.

In addition, repeated daily stresses and minor injuries add to IVDD over a lifetime. Nerlich et al. (1997) noted extrinsic and intrinsic factors affecting IVD

health. Extrinsic factors include both a sedentary lifestyle that reduces the amount of deformations experienced by the annulus, and hydrostatic pressure changes experienced by the nucleus weakening regeneration of the disc. Mechanoreceptors, triggered by movement to induce regeneration, are overloaded by extreme and excessive vibrations, while minor injuries extrude the IVD and irritate nerve roots exiting the spinal column, accounting for 10% of lower back pain episodes (Tubach et al., 2004). Traumatic injuries dislodge, herniate, or otherwise disrupt the IVD, inducing anything from mild degeneration to immediate destruction of the IVD. Intrinsic factors create systemic oxidative stress in the body, thereby affecting maintenance of the IVD, including diabetes, smoking, and vascular disease (Nerlich et al., 1997).

Finally, genetic abnormalities such as some forms of scoliosis or kyphosis can cause varying degrees of impairment (Giampietro et al., 2009; Goh et al., 1999; Hristova et al., 2011). Symptoms include back and neck pain leading to disability and in some cases diminished vital functions (Giampietro et al., 2009). While generally considered sporadic, more sever congenital vertebral malformations are often asociated with other chromosome abnormalities at a frequency of 30 to 60% (Jaskwhich et al., 2000; Wynne-Davies, 1975),

While many people with IVDD can be asymptomatic, it is not uncommon for the degenerated discs to cause significant pain, making it one of the leading causes of work-related disabilities (Watson et al., 1998). Unfortunately, key aspects that can improve its intervention are not well understood. Many physicians begin treating chronic lower back pain or traumatic injuries with

physical therapy or pharmaceutical treatments including cortisone (Palepu et al., 2012). If these therapies fail to alleviate the pain, surgeries that remove the offending disc followed by either implantation of an artificial disc, or fusion of the motion segment (Schizas et al., 2010), typically reduce pain, but concominantly reduce spinal motion and increase the likelihood of complications with adjacent motion segments.

Through human cadaver and animal work, researchers have been able to better understand the anatomy, biomechanics, kinesiology, and microstructure of the disc (Raj, 2008; Roughley, 2004; Schnake et al., 2006; Setton and Chen, 2004; Walter et al., 2011; Zhao et al., 2007). Unfortunately, once the IVD is damaged, clinicians and researchers are still unable to understand the key underlying mechanisms needed to heal the IVD. In an effort to reverse IVDD and to avoid surgeries that fuse adjacent vertebra together, research has focused on artificial implants, gene therapy, and growth factors that may stimulate disc remodeling and reduce pain (An et al., 2003; Barbir et al., 2011).

However, Ramos et al. (1994) applied 445 N of mechanical traction (i.e., distraction) and measured intradiscal compressive pressures below -13.33 kPa (Ramos and Martin, 1994). Computed tomography images have shown distraction increases the intradiscal space causing a negative pressure, which in some cases restores the structure of a herniated disc (Onel et al., 1989). A research group led by Kroeber (Guehring et al., 2006; Kroeber et al., 2005) demonstrated the ability to regenerate the disc of a rabbit. In their study, they first used a device to compress the disc and caused it to degenerate. They then

altered the same device to apply distractive forces to the vertebrae and subsequently to the IVD. When compared to the degenerative discs in compression, their work showed that disc distraction may help the disc to remodel, showing increased disc thickness and increased striation of the annulus architecture.

Distraction techniques are widely used by physical therapists and chiropractors to alleviate lower back pain. Typically, a person lays on a split table (Figure 1.2). An abdominal strap constrains the upper body to a fixed table section. A computer-controlled loading mechanism pulls on a strap attached to the pelvis situated on a sliding table section. Altering the position of the legs or back in various ways is expected to change the target level in the spine. Distraction loading amounts, length of therapy sessions, and treatment regimens vary greatly and are typically not based on data. The general loading pattern,

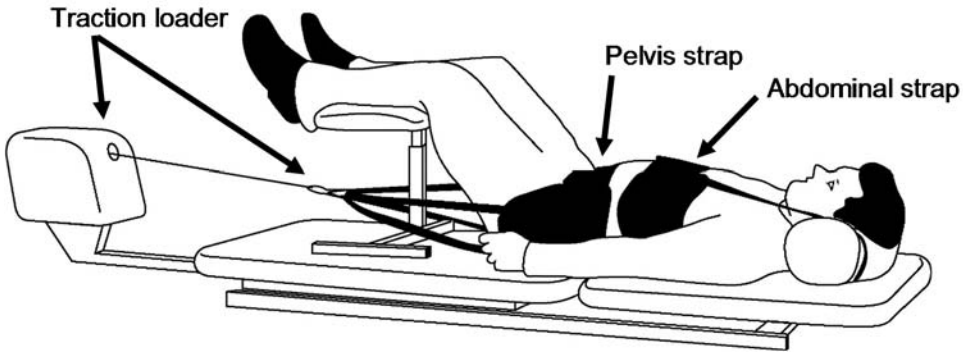

Figure 1.2: Traction tables are built with varying degrees of complexity to offer increasing numbers of possible positions. Changing the height of the support holding the legs or placing pads under the thorax are simple ways to change the target level of the spine. Drawing based on a manufacturer photo of a DJO Chattanooga TTET-200 Traction Table.

however, is shown in Figure 1.3 and consists of intensive cyclic loading for 2 weeks and tapering off over approximately 6 – 8 weeks (Geiringer and deLateur, 1990; Saunders, 1983; Swezey, 1983).

Human cadaver studies indicate distraction reduces pressure in the intervertebral disc. Human *in vivo* research, however, have been limited by low sample sizes, flawed experimental designs, and inadequate patient-based surveys (Fritz et al., 2010; Gay et al., 2005; Gay et al., 2008; Geiringer and deLateur, 1990; Saunders, 1983; Swezey, 1983; van der Heijden et al., 1995). In a literature review of 24 such studies regarding traction, van der Heijden et al. (1995) found no conclusive clinical evidence of the efficacy or conversely the ineffectiveness of traction therapies. Another review of 30 distraction studies by Gay et al. (2005) discovered similar findings and concluded further research was needed to determine biomechanical and neurological mechanisms as well as establish safe practices that maximize therapies (Gay et al., 2005).

Developing and conducting conclusive *in vivo* studies on humans regarding traction is difficult. IVDD screening typically uses radiography to assess degeneration by measuring the distance between adjacent vertebrae, while

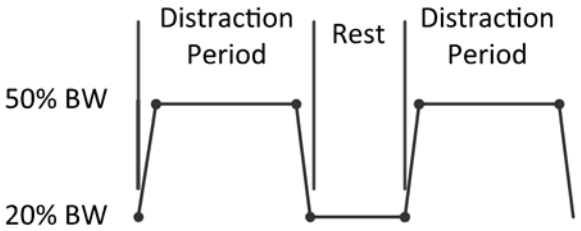

Figure 1.3: The body weight (BW) of the individual determines the cyclic distraction loading with generally accepted ranges of 20-50%.

magnetic resonance imaging (MRI), the gold standard in soft tissue imaging of the IVD, provides a conclusive diagnosis by comparing the hydration and morphology of the IVD (Adams et al., 2002; Thompson et al., 1990). The higher cost of MRI compared to radiographs prohibits its use for most research studies; however the lack of available *in vivo* human biochemical markers and difficulties isolating human IVD for targeted therapies hampers all human studies. For *in vivo* spine research that provides reduced imaging costs, opportunities to assess the physiology and accessible motion segments, animal studies are often suitable substitutes.

1.2. Animal Models

The effects of load and distraction on disc degeneration have been extensively researched with rat-tail models, due to several rather appealing attributes. The rat-tail represents an extension of the spine with motion segments beyond the fused sacrum (Figure 1.4), allowing for direct comparisons to the upper levels of the rat spinal column. Furthermore, the spinal cord ceases to pass through the center of the vertebra in the tail. Instead, the spinal nerve splits into four nerve tracts before the fourth caudal vertebra (C4) then follows the length of the vertebrae (Schaumburg et al., 2010). Well-designed methods take advantage of the interval between the vertebrae and nerves to minimize the risk of neurological injury or undesirable neurological stimulation (Figure 1.5). The main advantage involves uninhibited access to vertebrae with minimal surgical trauma to the rat. Therefore, complete isolation and avoidance of disrupting the

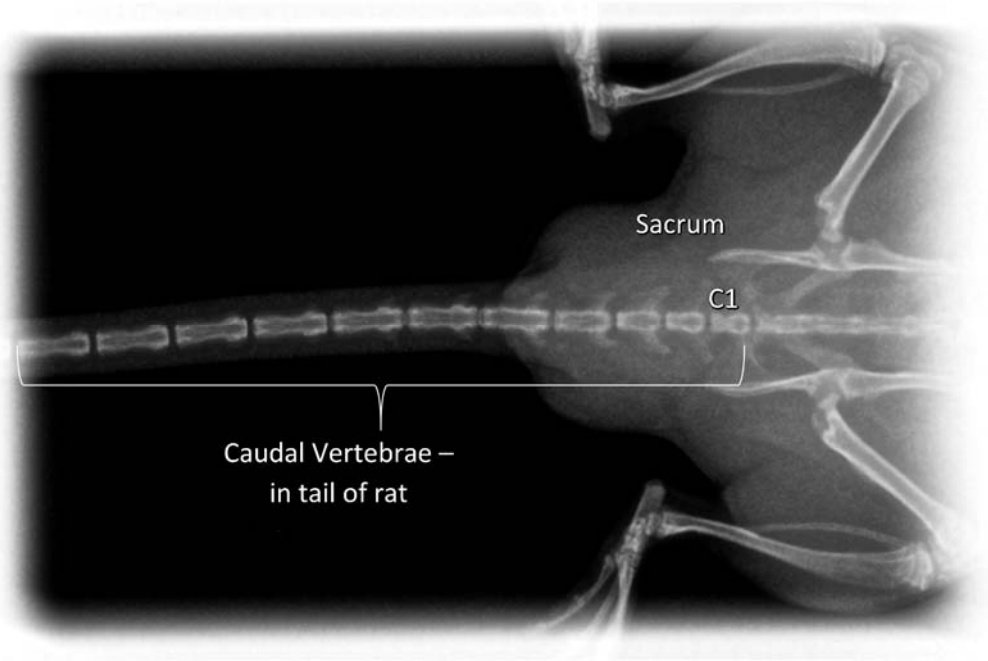

Figure 1.4: A radiograph of a Sprague Dawley rat shows the lack of background noise from other tissues surrounding the fused sacrum and caudal IVD often used for research.

loaded vertebra is possible, reducing the ability of surgical procedures to produce bony changes irrespective of the applied mechanical stimuli. Thus, the rat-tail offers a unique, practical, and well-controlled model for the study of intervertebral disc remodeling.

While limited by factors regarding the natural use of rat caudal discs and other physiological mechanisms, the rat-tail model continues to be regarded as suitable for human disc research in many situations (Beckstein, 2008; Elliott and Sarver, 2004; Lotz, 2004). Brent Showalter et al. (2012) compared the base

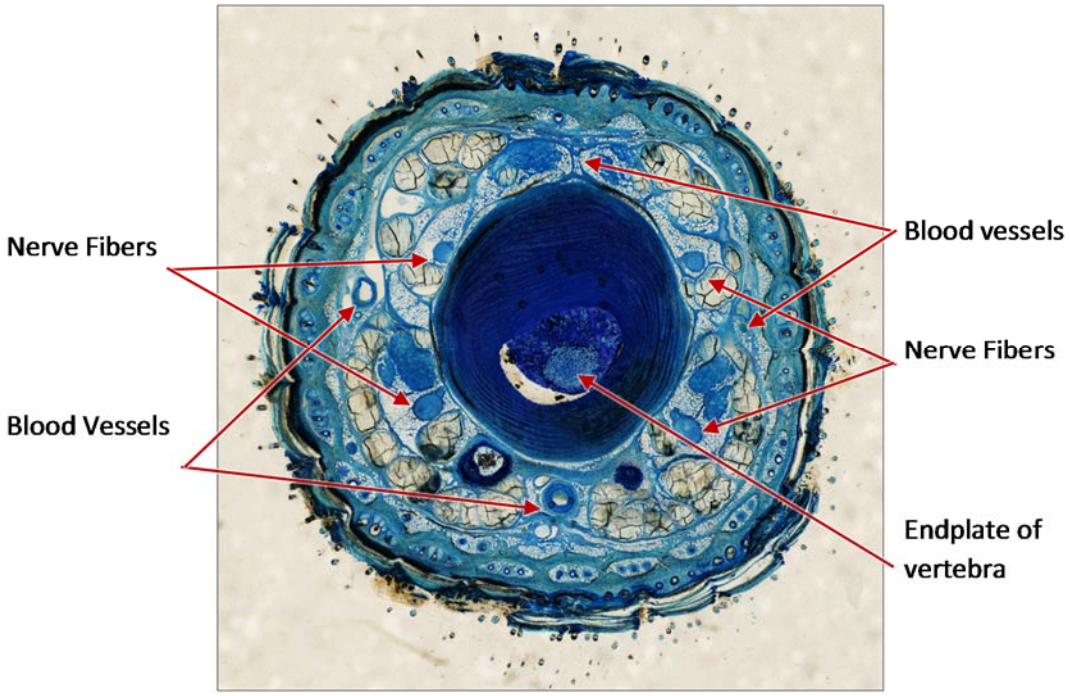

Figure 1.5: Alcian blue (pH 2.5) stained slide of a rat-tail cross-section guides the research by providing landmarks of nerve fibers and blood vessels running parallel to the motion segments (Luna et al., 1968).

tissue properties of intervertebral discs from several animals including rats and humans using axial compression mechanics and torsion mechanics. Normalizing the geometries of the animals to the measured loads and strains indicates the base tissue material properties are the same between the species (Showalter et al., 2012).

1.3. Ilizarov-type Device

Experiments using a rat-tail model to investigate compression on the IVD to induce degeneration frequently use an Ilizarov-type device. This type of device consists of two rings attached to vertebrae adjacent to the target IVD (Figure 1.6).

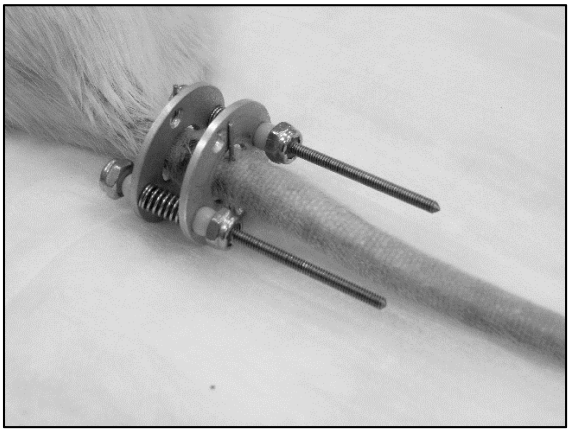

Figure 1.6: A scoliosis study exploring static distraction used an Ilizarov-type device similar to this one with stainless steel rods, screws, and nuts with aluminum rings. Rings are also molded from carbon fiber.

In a compression configuration, the rings are pulled together, either statically or dynamically (Akyuz et al., 2006; Maclean et al., 2004; MacLean et al., 2003; MacLean et al., 2008; Stinnett-Donnelly et al., 2007; Wuertz et al., 2009; Yurube et al., 2010). In a distraction configuration, the rings are pulled apart with a mechanical mechanism (Lai and Chow, 2010). All of the devices used previously for distraction include MRI incompatible metal pins, limiting *in vivo* imaging to radiographs when the pins are implanted. MRIs are clouded by artifacts from even nonferrous metals. Taken with an altered 7 Tesla MRI scanner (Model BioSpec 70/30 Bruker Inc., Billerica, MA) to avoid damage to the machine, axial images of stainless steel and titanium rods in saline-filled syringes create pronounced artifacts in comparison to a carbon fiber rod or the saline-only sample (Figure 1.7). Other measurements (histology, immunohistochemistry, and gene expression) require harvesting the disc from a euthanized animal. Metal

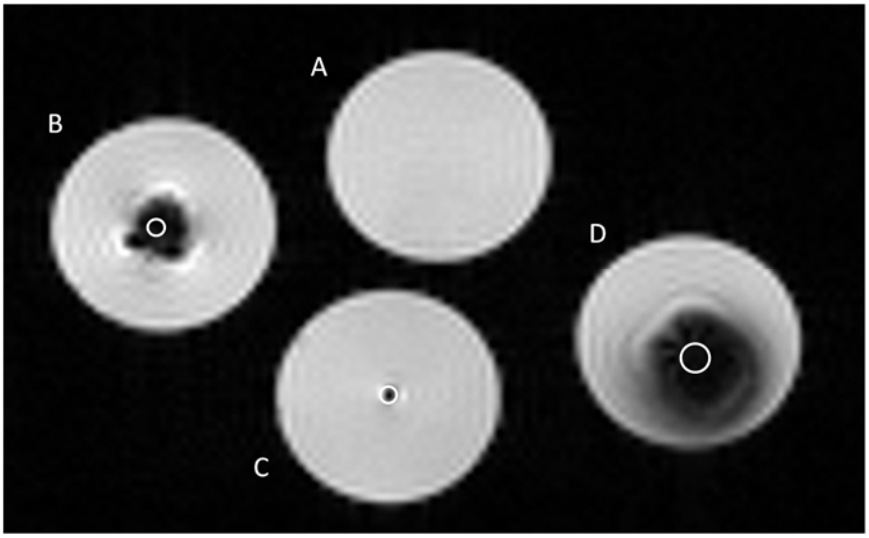

Figure 1.7: White rings indicating the size and placement of the metals and carbon fiber rod separate the object from the surrounding artifacts on a T1 MPRAGE image of (A) Saline control, (B) Standard stainless steel 0.76 mm (0.030 inch) Kirschner-wire, (C) Carbon fiber rod 0.76 mm (0.030 inch), and (D) Titanium screw.

problems aside, current *in vivo* MRI is limited to general morphology without differentiating the tissues of the disc. To take advantage of the soft tissue imaging capabilities of MRI and provide resolution that can differentiate the tissue of the rat IVD, a novel device made of nonmetallic materials would need to be developed. In this study, tools were developed to quantify the volume changes of different IVD tissues for *in vivo* rat-tail protocols simulating human practices.

In this project, we produced a system for distraction of a rat-tail intervertebral disc with nonmetal implants to use with the MRI protocol. First, an MRI compatible Ilizarov-type device was developed and mechanically validated. Second, a system to repeatedly manipulate the Ilizarov-type device for distraction of the IVD while the animal was alert and permitted removal of all but the

implanted rings when treatments were not administered was created. The distraction system was validated through mechanical testing with pressure and load sensors measuring the forces placed on the rings of the Ilizarov-type device by the distraction system. Finally, an MRI protocol was developed to provide distinction of disc tissues of live rats and validated by image comparison with animal postmortem histology. With these tools, researchers can gain insights into the mechanisms of intervertebral disc degeneration and regeneration through imaging before, during, and after treatments with live animals not previously attainable.

CHAPTER 2

DISTRACTION DEVICE

2.1. Device Requirements

To create a distraction system that can simulate human clinical settings, parameters must be established. Producing a distractive effect in humans is achieved with a minimum spinal elongation loading of 25% of the body weight of the individual (Judovich and Nobel, 1957). However, therapeutic IVD extension only occurs with loads greater than 50% of total body weight (Judovich, 1955).

The loads exerted on the IVD provide insights into the pressures experienced by the nucleus and annulus by dividing the loads by the cross-sectional area of the IVD. Elliot and Sarver (2004) reviewed 13 studies measuring human lumbar intervertebral disc area with different techniques and cohort numbers. For the rat-tail comparison calculations, the data from Fujiwara et al. (2000) were chosen from that review, because it was obtained using MRI rather than interpolated from bones and had one of the highest subject counts of 44 compared to 12 or less for 10 of the other 13 studies. The average cross-sectional area for 110 motion segments from the first thoracic to the first sacral vertebrae was 1390 mm^2 with a height of 6.4 mm and a lateral/anterior-posterior ratio of 1.39 (Fujiwara et al., 2000). For a 70 kg male sitting slouched in a chair,

the pressures in the IVD between the lumbar fourth and fifth vertebrae is calculated to be 0.27 MPa (Wilke et al., 2001).

Based on pilot studies for this project, an average 8- to 9-month-old, healthy male Sprague-Dawley rat had a mass of 525 g, and therefore, a 50% total body mass was 262.5 g or 0.2625 kg. The maximum loading was calculated by multiplying the gravitational constant (9.81 m/s^2) by the 50% body mass (0.2625 kg) to obtain 2.6 N. The average cross-sectional area of the caudal ninth and tenth vertebra (c9-10) IVD was 8.26 mm^2 for 12 mixed gender rats either 4 months old or 8 to 9 months old. The height of the average IVD was 0.90 mm and the lateral/anterior-posterior ratio was 0.96 (Elliott and Sarver, 2004). With a 2.6 N load on the tail, the intervertebral disc sustained 0.31 MPa. To simulate clinical procedures, the distraction system must sustain rat spinal loading of at least 2.6 N. A safety factor of 3 required structural failure greater than 7.9 N. Because the system was to be distracted with a closed loop control system, the distraction device could flex ±0.5 mm in the axial direction of the tail.

Previous research has used an Ilizarov-type device to transmit the compressive or distractive force from the exterior of the tail to the vertebra and IVD. The anatomy of the tail must be considered when implanting these devices. As stated earlier (Figure 1.5), the device must avoid disruption of the lateral, dorsal and ventral blood vessels or risk creating injury that may unintentionally modify the study or kill the animal. Perturbing the four nerve fibers in the tail hampers signals from mechanoreceptors in the ligaments and pain signals, which might otherwise trigger biochemical activities in the target IVD. If tendons

surrounding the IVD are not taken into consideration when implanting a device, the sinuous fibers could interfere with the rods of the Ilizarov device during insertion, causing harm to the animal and/or misdirect the implantation.

The irregular shape of the rat caudal vertebra dictates the required surgical instrumentation, preoperative planning, and choice of Ilizarov rods (Figure 2.1). Implanting the rods in a strict ventral-dorsal orientation or laterally positions the point of the drill bit on either the spinous process or transverse process of the vertebra. The drill bit points tended to deflect to either side of the process, missing the target line through the vertebra. To maximize the strength of the rod while minimizing weakening of the cortical bone, the rod should be no larger in diameter than the cancellous region between the cortical bone.

Any material implanted into the animal must be sterilizable, preferably either with an autoclave (for convenience and cost) or with ethylene oxide, and for use in MRI, reduce artifacts or constrain them to non-regions of interest. In a study of

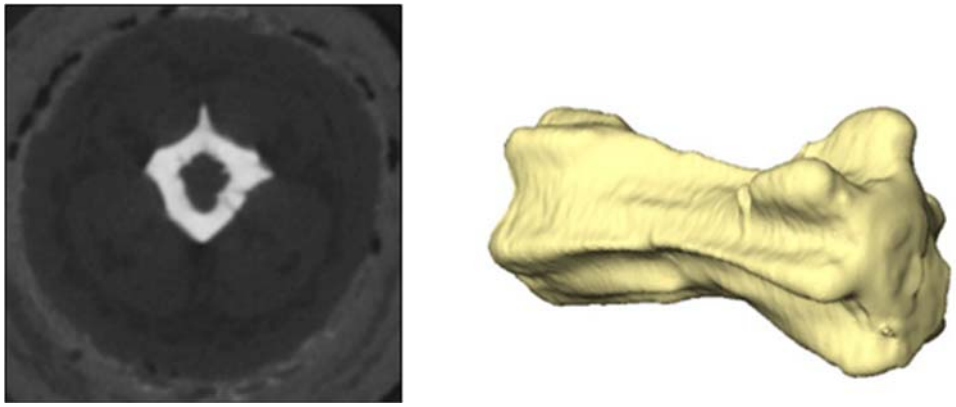

Figure 2.1: The median slice of a computed tomography (CT) scan of a caudal rat vertebra on the left combined with the 3D rendered segmentation on the right of the same CT scan illustrates the surface complexities that make drilling difficult.

16 polymer materials, only Ertalyte®, nylon 6/6, polyether ether ketone (PEEK), and polyphenylene sulfide (PPS) were considered to create background signals low enough to be regarded acceptable for use with MRI (Marjanska et al., 2008). Based on previous experience of this lab and others with implanted rats, materials that are implanted should be difficult for the rat to chew on, yet not harmful if ingested. An Ilizarov-type device permanently attached to the tail should be lightweight and provide maximum mobility. Materials chosen will take into account MRI compatibility, animal biocompatibility, and behavior concerns.

In order for the distraction device to be successful, it must be able to sustain 7.9 N, deform axially less than ±0.2 mm with an axial loading of 2.6 N, not injure vasculature and minimize neural disruption, and have minimal MRI artifacts in the region of interest.

2.2. Ilizarov-type Distraction/Traction Model

The Ilizarov-type device was designed based on a rat-tail IVD compression study by Walsh and Lotz (2004). In their device, they fixed one of the rings inside a cylinder and pushed the other ring towards it with a pneumatic bladder on the outside of the opposing ring (Walsh and Lotz, 2004). To create a distraction device, the process was reversed with a computer-controlled bladder in between the two rings. Based on a pilot study, the c6-7 IVD was chosen as the largest caudal IVD able to be imaged with the available MRI equipment. To begin the design, basic dimensions were taken from radiography of rat-tails from a previously approved Institutional Animal Care and Use Committee (IACUC)

study: c6 and c7 vertebra length 8.3 ±0.3 mm, center-to-center intervertebrae distance 9.0 ±0.3 mm, overall tail width 11 ±1.0 mm, and the diameter of the cancellous region at the center of vertebra 1.0 ±1.0 mm. With these measurements, the Ilizarov-type device used by Walsh and Lotz (2004) for mice could be modified and scaled for MRI of the rat-tail.

To reduce artifacts, lightweight carbon fiber rods were chosen. Rods with a 0.76 mm (0.030 inch) diameter, a size smaller than the average cancellous region between the cortical bone, were used to reduce cortical bone impact. The carbon fiber rods were 15% epoxy resin and 85% carbon fiber (Model 0.030 x 24 Carbon Fiber Rods, Midwest Products Co., Inc., Hobart, IN). A 0.76 mm diameter carbon fiber rod was 0.0073 g/cm or 0.0365 g for a 5 cm long rod. Carbon fiber exhibited no MRI background signal (Figure 1.7) and is biocompatible in many cases including orthopedics (Ali et al., 1990; Howard et al., 1985). When calculated with a three point flexural test, the theoretical deflection (Δy) is 0.0042 mm for a 0.76 mm carbon fiber rod with longitudinal tensile modulus (E) of 145 GPa, a length between support points (l) of 12 mm, a center applied force (F) of 4.5 N, and cross-sectional moment of inertia (I) of 2.65E-13 m^4 (Callister and Rethwisch, 2008; Hibbeler, 2008).

$$\Delta y = \frac{Fl^3}{48EI} \qquad [2.1]$$

For the device under development, one end of each 50 mm long carbon fiber rods was sharpened to a point with a scalpel blade.

The rings were created from polysulfone (Psf) (McMaster-Carr, Santa Fe Springs, California). Like the PEEK tested in the previously referenced MRI materials test (Marjanska et al., 2008), Psf, not included in that study, has good impact and tensile strength and no MRI background noise; however, it is four times less expensive than PEEK. Resistant to most hospital chemicals, Psf has a temperature range of -40° C to 140° C, can be sterilized, and is considered biologically inert as shown by its use for filtration in dialysis membranes (Dickinson, 1989). The tail width dictated a center hole of 12 mm to allow room for the largest tail size from a 654 g rat. The outer diameter of the ring, 26.38 mm, was minimized to reduce the size of the MRI coil, as will be discussed later, while allowing room for a bladder to be placed between the rings (Figure 2.2). The bladder was inflated within the grooves to distract the rings and incur a negative pressure on the IVD. Taking the vasculature and vertebra topography into consideration, the rods were placed at a 45° angle. Canting the rods created a near perpendicular interface between the rods and bone while increasing the distance from blood vessels. Placing the rods 85° from each other reduced the chance of damaging neural fibers (Figure 2.3). Machining prototypes demonstrated that drilling holes for the rods was best done before the groove for the bladder was cut as the drill bits tended to bend into the thinner space of the groove. The 3.15 g per Psf rings allowed the rat maximum mobility in terms of weight and the rings' size allowed motion segment flexion and extension.

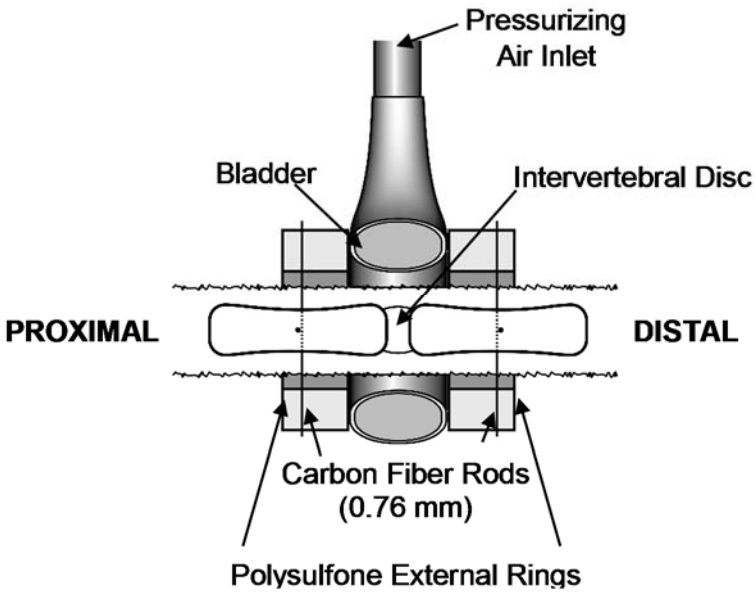

Figure 2.2: A removable pressurized bladder between the two rings of the Ilizarov-type device distract the vertebrae extending the IVD.

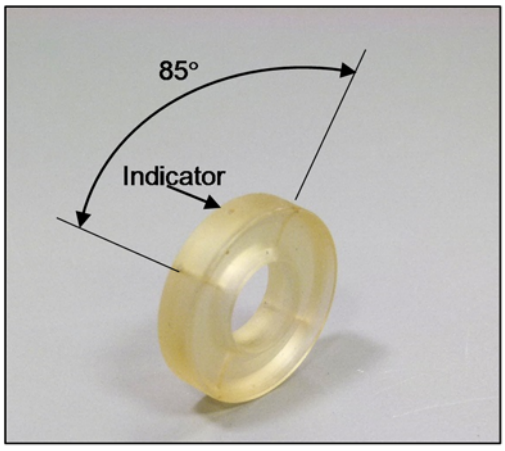

Figure 2.3: The semitransparent Psf ring allow visualization of the rods and a small hole in the top aided in orientation of the 85° side.

2.3. Surgical Implantation of the Ilizarov-type Device

Following institutionally approved protocols, five animals were used to develop the surgical procedures with three motion segments from each animal. Focus was placed on the motion segment intended for distraction studies: c6-7.

In order to avoid vasculature and nerves, the rods were inserted at an angle. At the median of the vertebra, the surface planes of the bone and critical systems required a nonperpendicular drill bit entry. Because the 0.76 mm (0.030 in) twist drill bits are thin, they bend and do not stay in position when encountering a nonperpendicular surface. Traditional K-wires were better because they do not have flutes, which make them stiffer; however, in our tests, the 50° and 80° angle still made it difficult to keep the wire on point. We machined tri-pyramidal stainless steel wires with a maximum point angle of 25° (Figure 2.4). Using a solid wire instead of a twist drill bit with flutes reduced the

Figure 2.4: Tri-pyramidal drill bits cut with the outside edge of the faces and the point guides the drilling process reducing movement of the bit off of the target line.

amount of tendon adsorption to the bit and wrapping around it. Further reduction from tendon wrapping came from drilling in a clockwise 180° to counterclockwise 180° in a back and forth motion. Cut to 50 mm, the bits ensured complete penetration through the tail and ring as well as something for a pin vise to attach to. Minimizing the length reduced the amount of bending in the bit while using a manual pin vise.

To implant two rings in adjacent vertebra with rods penetrating the vertebra through the center of the bone, ensuring the rings parallel alignment to each other and perpendicularity to the tail, an alignment bed was created (Figure 2.5). The bed incorporated adjustments for animal placement and ring offset shims to precisely place rods in the vertebrae. Slots for the rings and set-screws eased

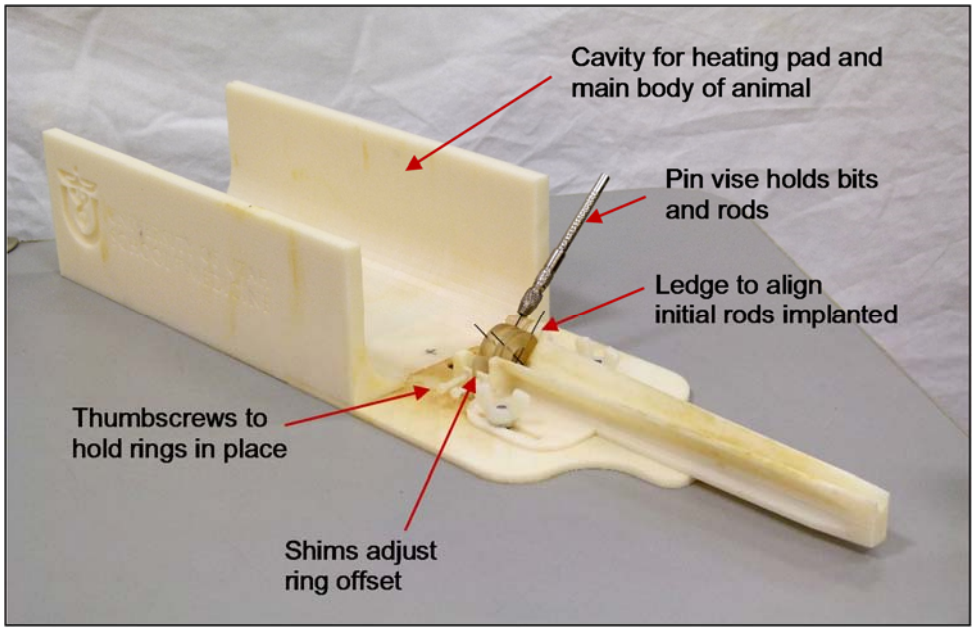

Figure 2.5: The installation device positions the body of the rat with a heating pad in the U-shape on the left, while the tail is positioned in the groove of the device on the right.

removal of the rings and animal. An alignment ledge ensured rods enter the vertebrae at the desired angle as described previously. Dimensions allowed for a pliable all-polymer water circulating heating pad to be placed under the animal to maintain thermal homeostasis during the surgery. All of the device pieces except for nylon screws (McMaster-Carr, Santa Fe Springs, California) were fabricated with a 3D printer (Model Dimension Elite, Stratasys Ltd. Minneapolis, MN) from acrylonitrile butadiene styrene (ABS). Fluoroscopy usage for vertebra detection was enhanced by reduction of material in the surgical region.

The tri-pyramidal point was ground using the rotary attachment on a benchtop milling machine (Model 5400 Deluxe Vertical Milling Machine, Sherline, California) to hold the wire and incrementally rotate it 120 degrees. In between rotations, the y axis held the point against a grinding stone on a rotary tool (Black and Decker, New Britain, Connecticut). The rotary tool was held stationary in a stand with the grinding stone at 12 degrees to the wire.

Surgeries were performed under sterile conditions with two packets made for each animal. The autoclaved packet contained a surgical towel and sponges while the ethylene oxide sterilized packet contained 5 drilling rods, 6 carbon fiber rods, and 2 rings. Sterile surgical gloves, gown, mask, cap, and shoe covers were worn by the surgical team. The heating pad in the alignment jig was set to 37 C and sterile towels were placed beneath and over the animal to aid in heat retention. The animals were anesthetized with 3-5% isofluorane, and a drop of eye lube (Model Optixcare, Optixcare, Canada) placed on each eye reduced dryness from the draft coming from the isofluorane setup. Anesthesia was

checked with a toe pinch. The surgical site was prepped with alcohol followed by a betadine solution. The tail was positioned through the rings of the alignment bed and the target disc located with a fluoroscope (Model GE6800 Mini C-ARM, GE Healthcare, Salt Lake City, UT). Twisting a pin vise holding a stainless steel custom bit back and forth, a hole was created in the vertebra. The stainless steel bit was quickly extracted and a carbon fiber rod held in a pin vise was inserted in the hole. The initial rod pushed the tail to the lower half of the ring; therefore, it often required sliding it upwards slightly on the rod. The second rod of the ring was installed in like manner as the first and the second ring also. Protruding sections of the rod were clipped with a microdiagonal clipper followed by pressing the remaining rod into the hole until it was countersunk by 1 mm. The set-screws were loosened and the rings and tail extracted from the alignment jig. The other protruding rods were cut and pressed into their holes to a 0.5 mm depth.

2.4. Ilizarov-type Device Validation

Testing the shearing properties of the carbon fiber rods when implanted in a maple wood dowel provided base information regarding the rods and rings while *in vitro* rat-tail testing provided a tissue comparison. Rings were implanted on a 3 mm diameter maple dowel with longitudinal grain (Figure 2.6). One ring was fixed to the base and the other ring attached to the 111.2 N (25 lb) tension/compression load cell (Model LCM300, Futek Inc. Irvine, CA) on a servo-hydraulic material testing machine (Model 1331, Instron Corp., Norwood, MA). To

Figure 2.6: Rods mounted in a maple wood dowel in the same manner as they would be implanted into a rat-tail hold Psf rings in place. For testing, the bottom ring is fixed with pointed screws to a baseplate.

simulate 8 to 13% strain for disc heights 0.8 to 1.2 mm, the rod/ring/dowel construct was preconditioned with a 1Hz sinusoidal cycle at ±0.1mm for 120 cycles followed by 120 s rest and a ramp test set by the testing control software (Model WaveMatrix, Instron Corp., Norwood, MA). Three constructs were tested with a ramp load rate of 0.05 mm/sec and a sample rate of 100 Hz.

Data on tissue behavior with the ring and rod construct were obtained with *in vitro* rat-tails of varying degrees of disc degeneration obtained from IACUC approved protocols. Carbon fiber rods and Psf rings were implanted in the c6-7 motion segment of two 12- and 13-week-old male Sprague-Dawley rats and two 12-week-old male Sprague-Dawley rats with 69 days of degeneration following

annulotomies and tested according to the previously described protocol for the wooden dowel.

The loading curves for the dowel tests were uniform with variation in the failure point 68.96 ± 5.64 N (Figure 2.7) with a displacement higher than anticipated of 0.22± 0.025 mm at 4.5 N (Figure 2.8). In these preliminary tissue tests, some tissue failure appeared to begin with 20-30 N loads. This was confirmed in later tests with only the IVD connecting the vertebrae. Ultimate failure of the tail occurred as high as 68.4 N due to the tough layer of skin.

The modulus of the dowel construct was 31.7 ±2.6 N/mm while the tissue was 6.5 times less at 4.9 ±3.3 N/mm. With a load of 2.6 N, the dual ring/rod

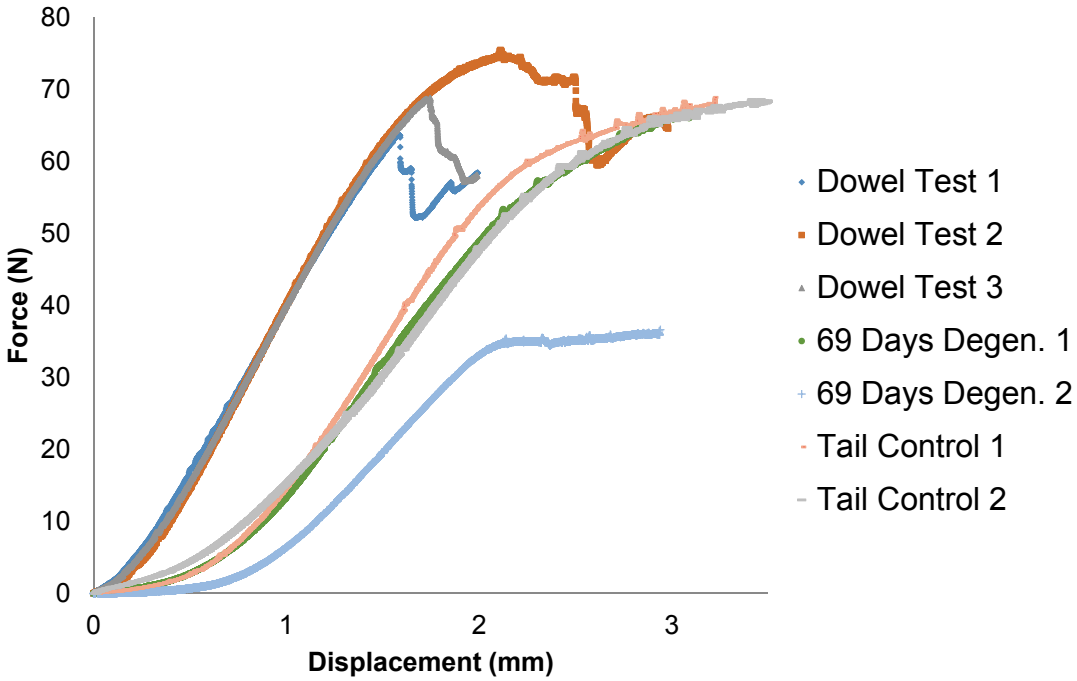

Figure 2.7: The dowel tests were uniform with higher failure points than the tail tests, which varied with undulations indicating points of tissue failure.

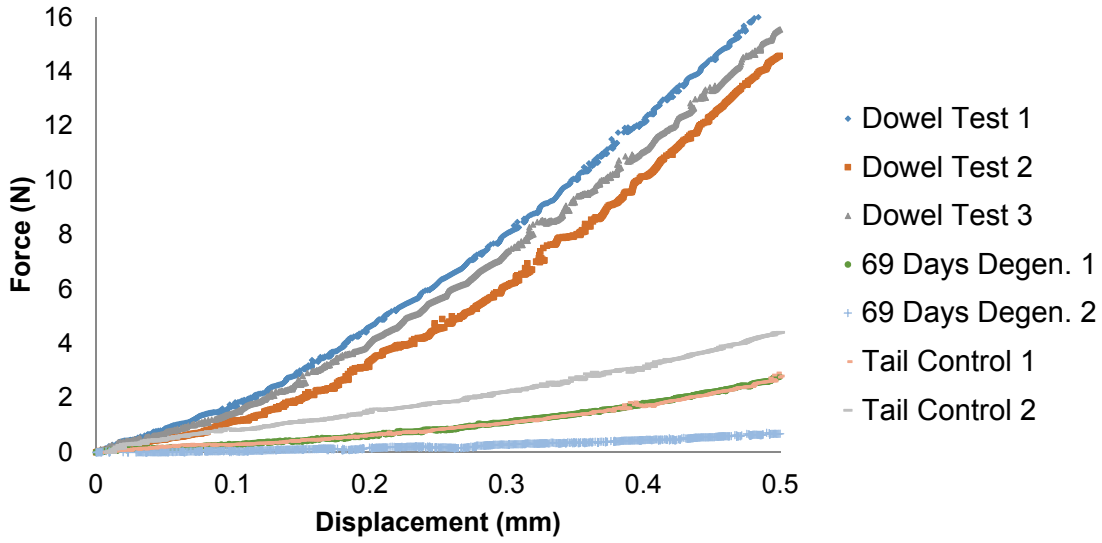

Figure 2.8: An examination of the toe region (0.0 – 0.5 mm displacement) containing the forces to be used in distraction studies illustrated the divergent tissue data and uniformity in the dowel tests.

construct attached to the dowel flexed 0.15 ±0.02 mm. The stiffness of the carbon fiber-laced rings was acceptable as the distraction force was maintained by a feedback load-controlled pressure system rather than a static force system.

In a distraction study using a rat-tail model, 40 animals were implanted with the Psf rings using carbon fiber rods and there were no fatalities or difficulties from the surgeries. Concerns arose 2 weeks after implantation from chronic inflammation around the percutaneous sites. Antibiotics reduced the inflammation, however the chronic foreign body response prompted continuous antibiotic administration over the length of the 6-month study. The inflammation could be from release of carbon fibers. Using rods with a greater epoxy to fiber

ratio matrix or coating the rods with an epoxy or cyanoacrylate may reduce these issues.

The device succeeded in achieving the study goals. It failed at 68.96 ± 5.64 N, 8.7 times the required 7.9 N. With a 2.6 N load, the axial deflection of the dual ring assembly was less than the desired ±0.2 mm at 0.15 ±0.02 mm. Surgeries designed to avoid the vascular and neural systems implanting the distraction system were conducted on 40 animals, resulting in zero deaths or complications directly resulting from the surgeries. Materials used were chosen to minimize MRI background noise or impact in the regions-of-interest and will be shown viable in Chapter 4.

CHAPTER 3

PNEUMATIC DISTRACTION SYSTEM

3.1. System Requirements

Based on the distraction device set forth in Chapter 2, the system to provide distractive loading must be a pneumatic system inflating and deflating the bladder in between the rings of an implanted Ilizarov-type device. Following the requirements of the distraction device, the system must provide a cyclical distractive force between 1.0 N and 2.6 N ±0.4 N for 20% to 50% BW of a 525 g rat. While there is no standardized protocol for distraction, an interview with a local practicing chiropractor revealed typical loading is conducted with a pseudo square wave pattern of 10 to 40 s of loading with 20 s of rest in between (Massengale, 2012); therefore, the distraction system must allow for programming the same loading criteria with a 0.5 s maximum change. As animals have varying body sizes, the system pressurizing the bladders must be flexible and adjust for pressures in the bladder based on the animal's size and movement.

To monitor the animal's reaction to the treatment, the animal must be free to move about an enclosure un-anesthetized. To allow the animal maximum mobility outside of treatments, reduce MR artifacts, and reduce fabrication, the

distraction system must be removable from the implanted distraction device that one machine can be used for multiple animals. It also must treat up to eight animals simultaneously to expedite treatments of animals in a study.

3.2. Hardware

For convenience and flexibility for this and future projects, a digital acquisition system (Model CompactDAQ, National Instruments, Austin, TX) was used with complimentary control creation software (Model LabView 2012, National Instruments, Austin, TX). An analog output module (Model NI cDAQ 9264, National Instruments, Austin, TX) would provide ± 10 VDC to control 10 solenoid pneumatic valves (Model MPYE-5-M5-010-B, Festo Esslingen am Neckar, Germany). The pneumatic valves were already in inventory from other projects and had proven well-suited for this project by a previous biomechanical testing system (Henninger et al., 2012). The pneumatic valves were two way and therefore could pressurize the bladder as well as release pressure. To fit with the tubing and connectors available, price, and less than 2 ms response time, voltage output pressure transducers (Model MLH 050PGL06E, Honeywell, Morristown, NJ) were chosen to provide feedback through an analog input module (Model NI cDAQ 9205, National Instruments, Austin, TX) with 16 bit samples at a rate of 250 kS/s to the control software. The pressure transducers were excited with 15 V from an transducer power supply (Model PSS-15, Omega Engineering, Inc., Stamford, CT) while power for the pnuematic valves came from a 10 V power supply. LabView 2012 running on a laptop (Model Thinkpad

W500, Lenovo, Beijing, China) was connected to the input and output analog modules through a 4-slot USB chassis (Model NI cDAQ-9174, National Instruments, Austin, TX) (Figure 3.1).

With pressure levels below 69 kPa (10 psi), pressure sensors in the aforementioned system measured ±20 kPa (3 psi) fluctuations in the University of Utah Othopaedic Research Center's building compressed air system. Therefore, the air system utilized K-size air tanks of capacity 43.3 L of air at 21 C 1 ATM and an on-tank regulator set to 689 kPa (100 psi). At the device, a regulator that controlled the maximum pressure fed into the distraction bladders, 55 kPa (8 psi). The on-device regulator pressurized two pressure vessels, 12.7 cm x 30.5 cm (5 in x 12 in), 1724 kPa (250 psi) air max. (TRD Manufacturing, Inc., Machesney

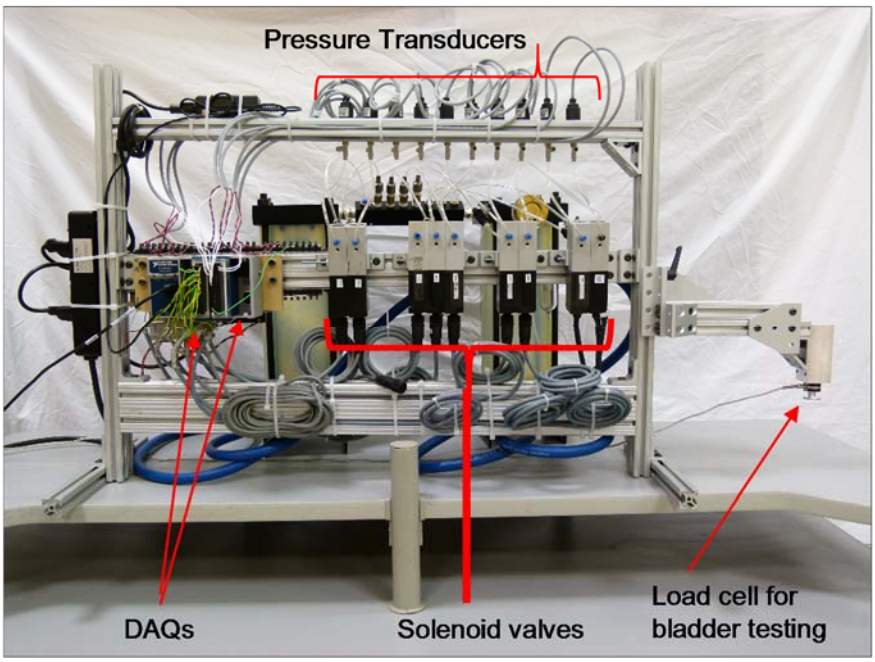

Figure 3.1: An 80-20 aluminum rack organized the components of the pneumatic control system and formed the framework for the bladder loading tests.

Park, IL), which sent air into both sides of a manifold (Model PCM20-250-08B, Polyconn, Plymouth, MN) (Figure 3.2). Air traveled to the solenoid valve by way of a 4 mm tubes with an inline thumbscrew adjusting valve and push-to-connect connections. Despite the on-board pressure vessels to reduce fluctuations in the air pressure across the manifold outlets, each valve outlet still required adjustment. The computer-controlled solenoids dictated the air pressure in the bladders using the feedback from the pressure sensors.

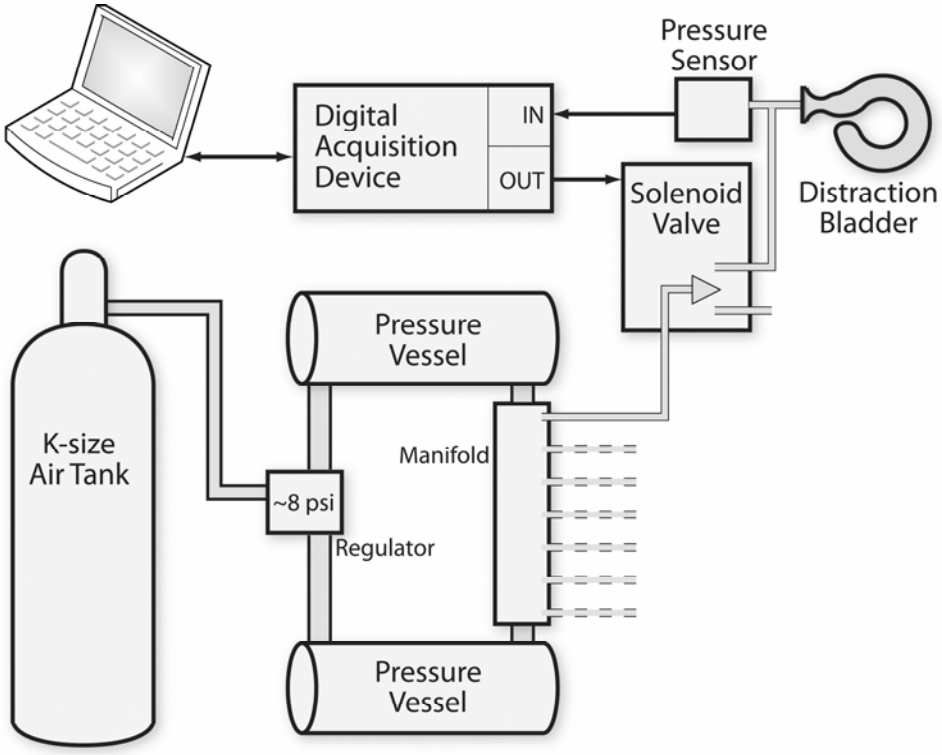

Figure 3.2: The structure of the pneumatic distraction system allowed for one to eight animals to receive treatments at the same time with the possibility of each one having a different treatment.

3.3. Software

Controlling the pressure in the bladders through the solenoid valves was a custom application created with control creation software (Model LabView 2012, National Instruments, Austin, TX). Bladder pressure from a pressure transducer on each bladder line was sent to the DAQ Assistant in the LabView code at a sampling rate of 1.5 kHz. Increasing the sampling rate from the initial of 1.0 KHz improved the system's response to changes. Increasing the rate further would likely improve the response; however, 1.5 KHz was the maximum attainable with the system as constructed. The pressure sensor data (process variable (F)) and desired pressure values (setpoint (S)) entered a proportional-integral-derivative (PID) controller based on the LabView PI.vi. The difference between S and F is the error (E) and P is the proportional constant, I the integral constant, and D the derivative constant.

$$\begin{aligned} O = O_{t-1} &+ D\big(E_{t-1} - (S - F)\big) \\ &+ (0.006 * 0.5 * I + P)E_{t-1} \\ &+ (0.006 * 0.5 * I + P)(S - F) \end{aligned} \qquad [3.1]$$

Because the center point of the valve is at 5 V, the output to the valve (O) was increased by 5 V: deflate 0-5 V and inflate 5-10 V. Using LabView-provided setpoint code, the desired value could be set as any value at any time point; thus, the output can be static, increased, decreased, changing or any combination of linear changes. In addition to the voltage output to the solenoid valve, data containing the setpoints and pressure sensor values for each line were output to a text file for later analysis.

To provide initial force values for the bladders and test their variability, additional functions for testing with load cells were added. The offset for the load cell and the loading/voltage output slope were incorporated to allow force measurements of a pressurized bladder.

3.4. Bladder and Collar

Reproducible flexible bladders were required for consistent results with minimal loading variability when pressurized to provide forces below 10 N in the rod/ring construct. A solution of 2 ml of water and 36 ml of latex rubber (Model C1204, Woodland Scenics®, Linn Creek, MO) was developed to create the custom bladders. Forming the bladders was done using a custom mandrel. One end of a 450 mm long by 9.5 mm diameter 304 stainless steel rod was turned to form the basic shape of a thick portion for the body of the bladder and a thinner portion to form the neck that could be zip-tied around the end of the air tube (Figure 3.3). The total length of the turned portion was 75 mm with the 6.5 mm

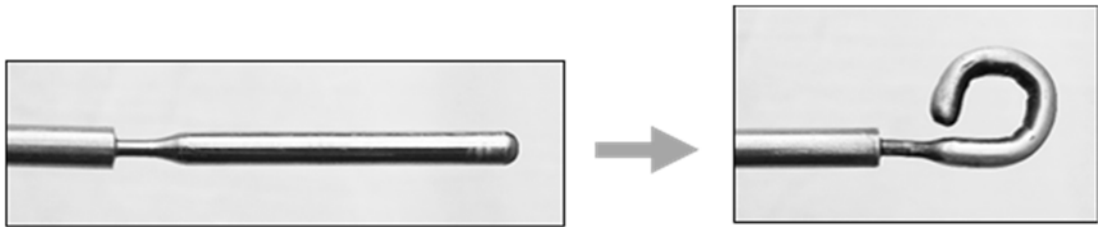

Figure 3.3: The total length of the turned portion was 75 mm with the 6.5 mm thicker portion consisting of 62.2 mm of the length with a 3 mm radius roundover, the 3.3 mm thinner portion comprising 6.7 mm, and a transition region between the thick and thin exacting the remainder. The tip was bent using a propane torch and hammer.

thicker portion consisting of 62.2 mm of the length, the 3.3 mm thinner portion comprising 6.7 mm, and a transition region between the thick and thin exacting the remainder. The turned portion was bent so the bladder would wind around the tail by holding the thick portion with a vise and heating a protruding portion of the mandrel to a “cherry red” with a propane torch (Model UL2317, BenzOmatic, Medina NY). The mandrel was then pliable enough to be hammered around a 12.7 mm metal rod. Sharp edges were removed with a fine file and 220 grit sandpaper.

Creating consistent bladders with a reasonable degree of reproducible pressurization required submerging the formed end of the mandrel at 2.4 mm/s in the latex solution and retracting it at the same speed to reduce bubbles and produce an even coat. After dipping, the mandrel was shaken for 1 minute over the latex container to dislodge excess material from the mandrel. Then the mandrel was held with the bladder portion upright for 1 to 1.5 minutes while bubbles were popped on the mandrel with a dry sharp implement (Figure 3.4). Periodically wiping off any wet latex from the sharp implement increased the implements ability to remove bubbles. The mandrel was inverted and held for

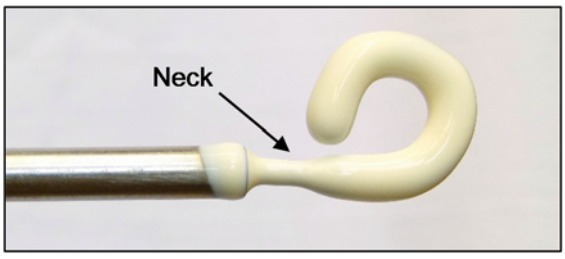

Figure 3.4: Additional latex applied around base of the mandrel reinforced the neck.

another 1-1.5 minutes allowing the latex to reflow and even the latex coating around the mandrel. The inverted mandrel with downward facing bladder was placed in a dehumidifier or other machine at 38 C and 2% humidity for 15 minutes or until the latex was translucent. The coating process was repeated one more time to achieve the desired thickness.

Applying facial powder (New York Color Smooth Skin Loose Face Powder 741A, Coty US LLC, New York, NY) liberally to prevent the bladder from sticking to itself, the bladder was removed from the mandrel. The outside of the bladder was first coated with facial powder followed by rolling the bladder onto itself starting at the neck. Continually coating the inside of the bladder eased the process and prevented the inside of the bladder from sticking to itself. After removal of the bladder from the mandrel, it was inside-out. The bladder was turned right-side-out by pushing the center of the bladder back through the center of the rolled outer edges of the bladder using a paper stick from a lollipop. The paper stick worked better than other implements tried as the paper slid against the rubber, was less likely to create holes in the rubber, and was the appropriate size. This created a 0.62 g bladder with a thin wall thickness of 0.32 ± 0.05 mm around the outside of the ring and a thicker wall in the center that maintained the shape of the bladder.

To contain the bladders as they were inflated between the rings, a collar that could wrap around the rings was required. In addition to containing the bladder, the collar allowed the rings to slide and provided a coupling point for the incoming air tube and the internal bladder. The collar also needed to be easily

removable to switch animals for treatments. Polysulfone was chosen to create the collar for reasons already cited. Collars were machined to an outer diameter of 39.6 mm and an inner diameter of 26.9 mm and a length of 35 mm. The collar was cut lengthwise and a 12.7 mm hole was drilled into the center of one of the sides for the air tube and to provide clearance for bladder attachment to the air tube with a 10.2 cm (4 inch), 80 N (18 lb) tensile strength zip-tie. The two sides were bound together with 20.3 cm (8 inch), 178 N (40 lb) tensile strength zip-ties and a drum sander shaped the interior to create a sliding fit with a Psf ring. A 3D ABS printed coupling was epoxied over the 12.7 mm hole in the collar (Figure 3.5) and electrical tape over one side of the main shell of the collar formed a hinge. On the opposite side of the collar, 20.3 cm zip ties wrapped in plastic wrap were generously epoxied to the collar. After the epoxy dried, the zip-ties were

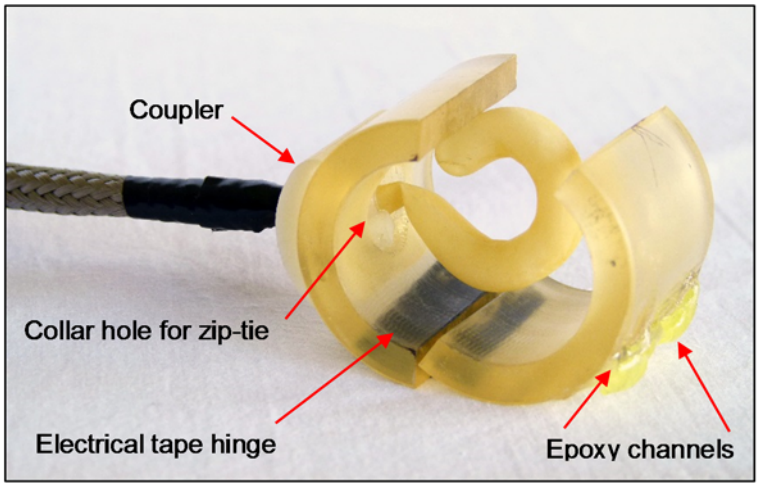

Figure 3.5: The hole in the coupler constricted the tube holding it in place. Pushing the tube in allowed attachment of the bladder. Pulling it back out positioned the zip-tie in the hole of the collar, allowing ring movement.

removed, leaving channels to maintain zip-ties used to bind the collar when attaching animals to the collar/bladder construct. Two centimeters of a 37 cm long 4 mm air tube were pulled through the coupling and the neck of a bladder was pulled over the end of the tube; a 10.2 cm zip-tie kept the bladder in place. A braided stainless steel sleeve pulled over the air tube kept animals from chewing through the tube and electrical tape wrapped around the end of the sleeve protected the animal from any sharp wires.

When installing the tail and implanted Ilizarov-type device in the collar, the tail was laid over the bladder with the end of the bladder facing up (Figure 3.6). A blunt object, such as closed forceps with a rounded tip, was used to wrap the tip of the bladder over the tail and down the other side. Zip-ties in the epoxy guides were pulled around the collar, pulled tight, and the remaining tie clipped with a diagonal cutter. One animal required several ties on the collar as he would chew

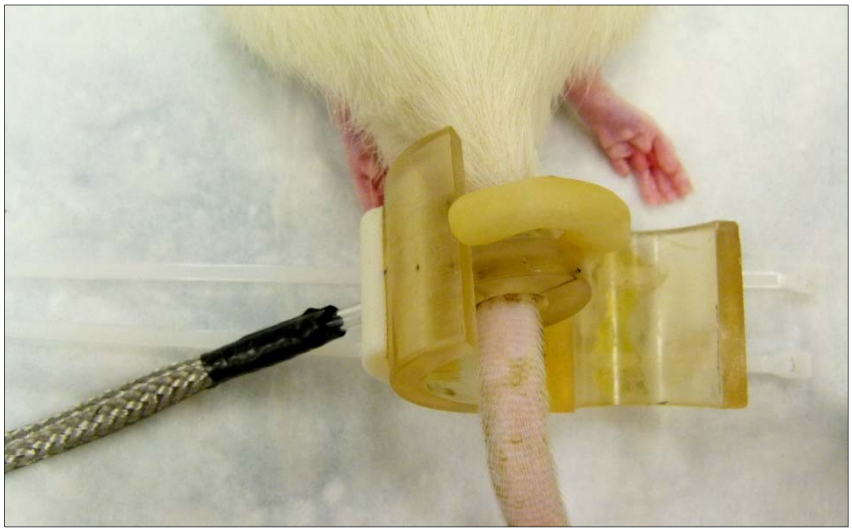

Figure 3.6: Animals were anesthetized while the collar was placed on their implanted rings.

them off during the treatments, despite no evidence of pain. The other end of the air tube was connected to a swivel connector in the top of clear 20.8 L containers (Figure 3.7) and a 1.5 m length of tubing connected the cage to the pressurizing device.

3.5. Distraction System Validation

The pneumatic distraction system was first set up and tested with a bladder between two rings in a collar with a metal post substitute for the tail and a metal ring spacer underneath the Psf ring. A 111.2 N (25 lb) tension/compression load

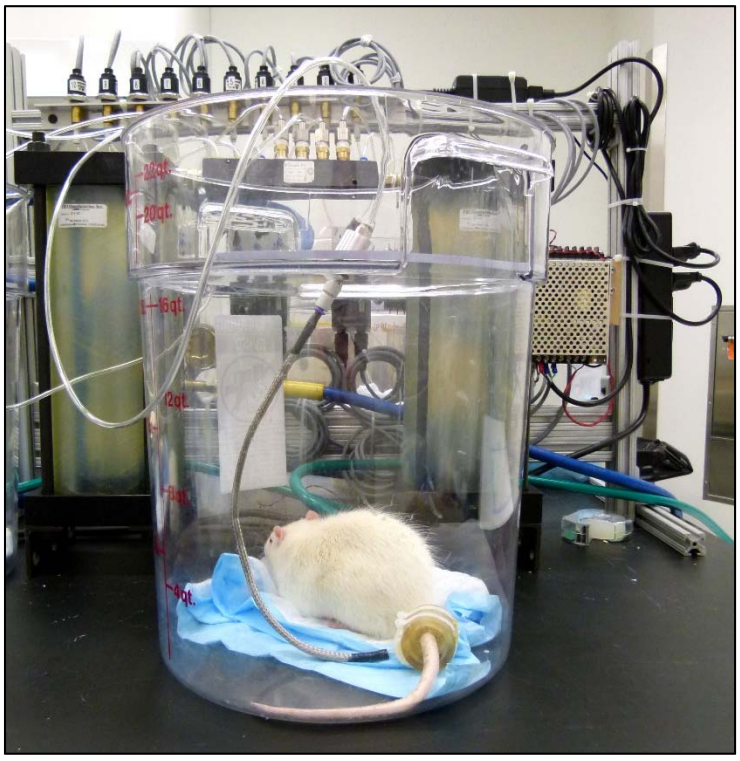

Figure 3.7: Upon collar placement, the animals were placed in a circular clear cage and awoke within a minute. The length of tube allowed them freedom of movement without entanglement.

cell (Model LCM300, Futek Inc. Irvine, CA) with a powered bridge sensor supply (Model DMD-465WB, Omega Engineering, Inc., Stamford, CT) was attached to a custom loading setup and input into the previously described custom control application through the analog input module. The voltage output of the load cell was zeroed and the calibration slope determined with 0.1, 0.5, 1.0, 1.6, 5.0, and 10.0 kg weights. A 5.03 g aluminum compressor plate attached to the bottom of the load cell was lowered until the bladder imposed a force on the load cell, then raised until the force was zero (Figure 3.8).

The controller was tuned using a 40-second step function with a 5-second rise and fall and 20-second rest (Figure 3.9) defined in the setpoint portion of the control application. Tuning the controller included, first, increasing the

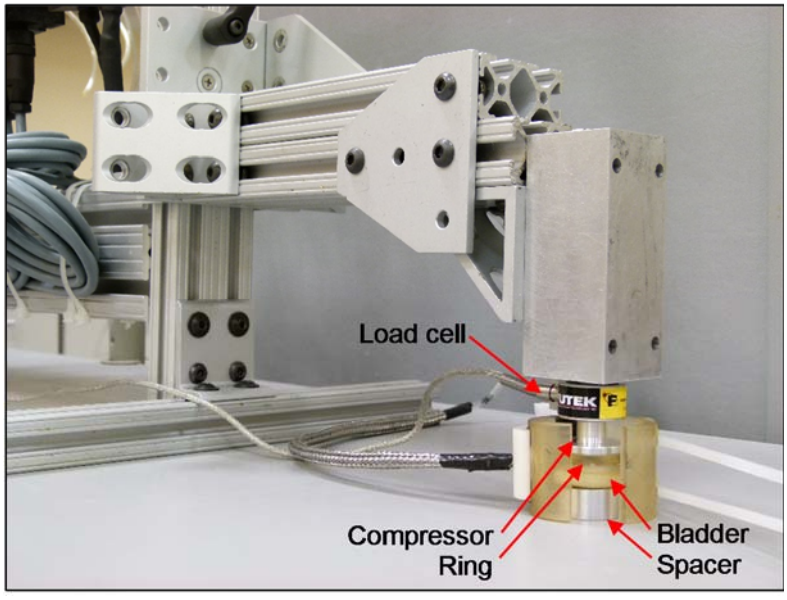

Figure 3.8: The distraction testing system allowed controlled bladder inflation, measurement of forces on the ring, and visual inspection of ring movement through the semi-transparent collar.

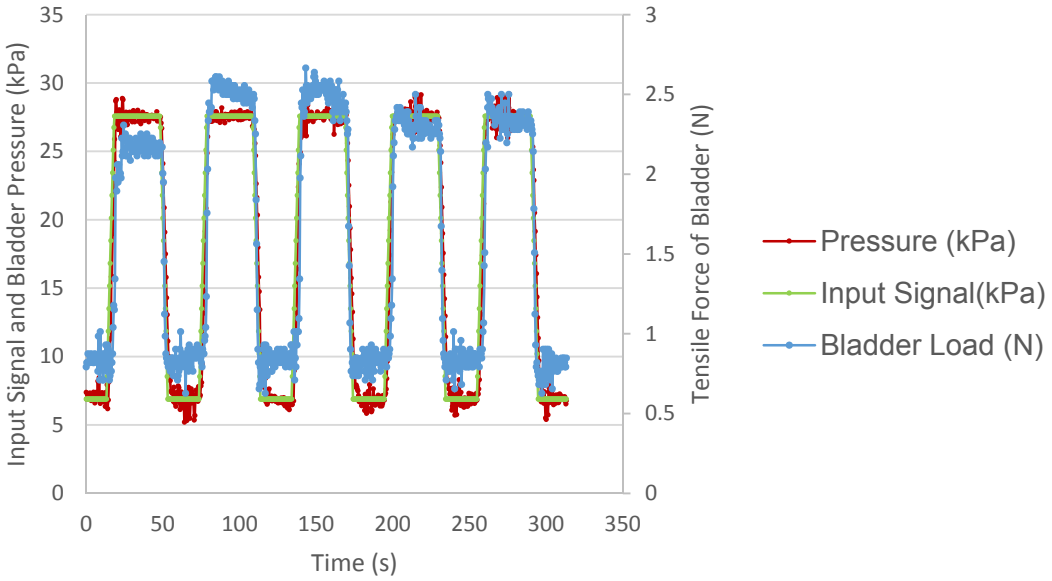

Figure 3.9: While the pressure tracked the input signal with some variation, ring loading imposed by inflation of the bladder had greater deviation.

proportional gain until the sensed pressure oscillated, then reducing the proportional gain until the oscillation stopped. Second, the integral constant was increased until the difference between the input signal and the sensed pressure was minimized or the system began oscillating, whichever came first. Lastly, the derivative constant was tuned in like manner to the integral constant. Tuning was done for each of the air output lines following adjustment of thumbscrew valves for variation in the lines from each other.

Bladders were tested for consistency by pressurizing the bladder with a ramp test at 0.46 kPa/s while measuring the force of the bladder against the load cell. In a test of 12 bladders, the pressure needed to achieve the target distraction force of 2.6 N was 30.04 ±3.10 kPa (Figure 3.10).

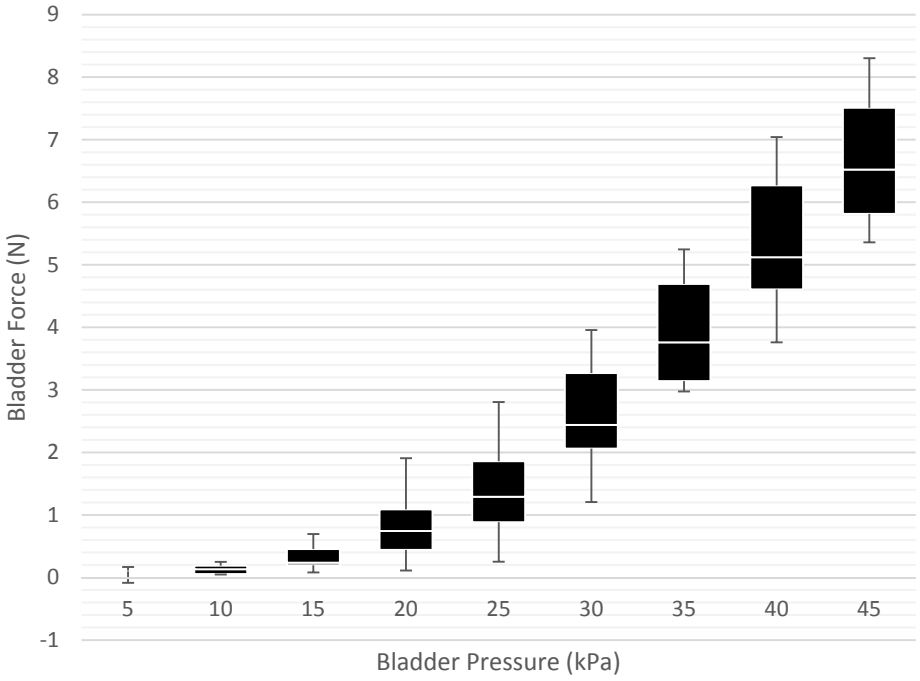

Figure 3.10: Experimental variations resulting from bladder differences in distraction studies are minimized by rotating animals through sets of bladders.

This study met the goals for designing, fabricating, and testing a new device that would provide distractive forces to a rat's caudal intervertebral disc by a pneumatic system inflating and deflating a bladder in between the rings of an implanted Ilizarov-type device. The system can provide a programmed cyclical square-wave type distractive force between 1.0 N and 2.6 N ±0.4 N with a maximum phase variance of ± 3 s between the programmed control signal and the load on the rings. The pressure sensor feedback control system adjusts to animals of varying sizes and animal movements. Visually and audibly monitored, un-anesthetized animals can move freely within an enclosure.

The distraction system is completely removable from the rat when not undergoing treatments, allowing the rat complete freedom and MRIs uninhibited by the distraction system. Up to eight animals at a time can receive distraction treatments to expedite treatments of animals in a study and reduce the number of systems to build.

CHAPTER 4

MRI IMAGING OF *IN VIVO* RAT-TAIL

4.1. *In vivo* imaging

For *in vivo* spine studies, radiography is often used to determine the health of an IVD by calculating the disc height index (DHI) (Figure 4.1). The height of the IVD is determined by measuring the distance between the vertebra across the disc space and normalizing it with the length of the adjacent vertebrae (Masuda et al., 2004). This technique is limited to quantifying changes in disc height, limiting analysis of soft tissue structures.

$$DHI = \frac{2(D+E+F)}{(A+B+C)+(G+H+I)} \quad [4.1]$$

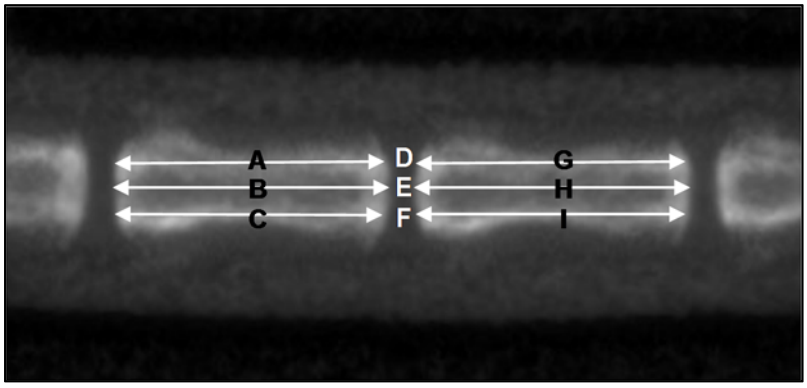

Figure 4.1: The disc height index uses multiple measurements to reduce the impact of bony variations and vertebrae misalignments.

To examine the health of the tissue, a T2 MRI scan is used to obtain a qualitative look at the water motility (i.e., water content) and morphology of the nucleus as determined by the Thompson grading scale or modified versions thereof (Masuda et al., 2004; Thompson et al., 1990). While imaging for water content does provide an indicator of the ability of the nucleus to withstand compressive forces, it is often limited by the use of the technology. MRI scans have an intensity gradient (Figure 4.2) related to the homogeneity of the transmitting and receiving radio frequency (RF) coil. When adjacent discs are compared to each other using a single T2-type MRI image slice, variations in the

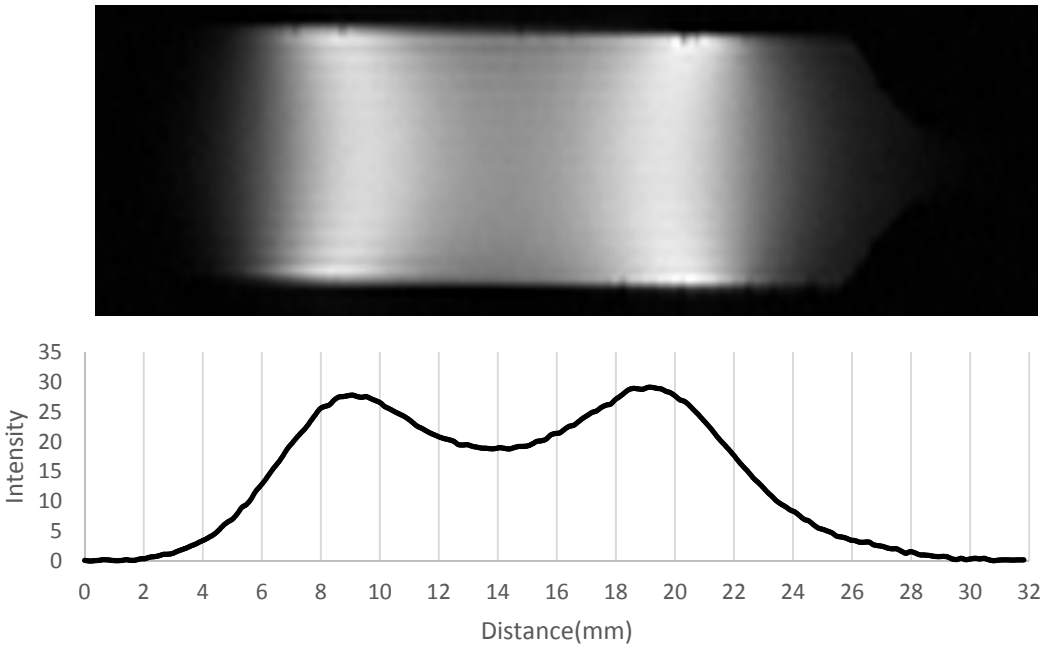

Figure 4.2: A syringe filled with saline shows the change in intensity despite a lack of change in material along the primary axis of a commercial 10 mm inner diameter (ID) quadrature coil. T2 MSME 40 x 40 mm FOV, 0.31 x 0.16 mm/voxel, ST 0.31 mm, TR 1000, TE 15, 1 Average.

intensity gradient can affect the conclusions. Using a T2–map reduces this concern by using multiple images of the same slice to interpolate and accurately quantify water content in the region of interest rather than relying on intensity values alone.

Another concern with relying on single-slice T2 imagery for the morphology in addition to water content depends on subject positioning. When MRI parameters are given, the slice thickness is often 2.0 mm. This attempts to obtain as much of the IVD in one image, allows for greater resolution, and reduces scan time. Depending on placement of the animal within the coil, the single slice may yield one IVD centered in the slice and perpendicular or parallel with the image plane while other IVDs are askew to the image plane and not providing an accurate comparisons.

Using a multislice T2-map to provide a 3D perspective of the water content, combined with a high-resolution T1 imaging protocol that focuses on the tissue morphology, the IVD can be accurately imaged for structural and osmotic integrity.

4.2. Commercial Coils

Subtle differences in soft tissues make MRI a key modality for IVD analysis. The high contrast sensitivity to those differences combined with volumetric data provides information that is difficult or impossible to obtain with other technologies. The use of nonionizing radiation is another reason MRI has replaced radiography for some studies, despite the high cost of MRI equipment

and maintenance, longer scan times than radiography, and technical complexities (Bushberg, 2012).

MRI is based on electrical current oscillations in the radio frequency (RF) range of MHz. The energy of atoms possessing nuclear magnetic resonance (NMR) properties or a magnetic moment can be changed by magnetic fields and generate an angular momentum. Hydrogen atoms (1H) are the NMR-active atom most widely used in MRI because the human body is 60% water (Guyton and Hall, 2006). The primary magnet (B_0) of an MRI aligns NMR-active atoms, and pulses from a perpendicular electromagnetic force, generated by an RF coil, excite hydrogen atoms. The RF coil can also receive the electromagnetic signal emitted as the atoms return to their previous state. Alternating currents in electromagnetic coils (gradients) localize the field for interpretation into an image space (Lauterbur, 1989).

RF coils are interchangeable within the bore of the primary magnet of an MRI system to suit the particular study. The sensitivity of an RF coil is directly linked to the quality factor (Q). The quality factor relates to the inductance of the RF coil or ability to create a magnetic field to the amount of energy lost in the field per cycle.

$$Q = \frac{2\,\pi(maximum\ energy\ stored\ in\ magnetic\ field)}{energy\ dissipated\ per\ cycle} \qquad [4.2]$$

or

$$Q = \frac{resonance\ frequency}{full\ width\ at\ half\ of\ resonance\ peak} \qquad [4.3]$$

An increase in inductance means a larger electromotive force, while less resistance in the system means less energy is lost in a cycle and the bandwidth is less disperse. The quality factor governs the total amount of signal generated versus the amount dissipated. A higher Q leads to a more sensitive coil.

Two other parameters are formed by the coil characteristics as well as the imaging protocol. The first is the filling factor (η) and the second is the signal-to-noise ratio (SNR). The filling factor is the ratio of the volume of the sample (V_s) to two times the interior volume of the resonator (V_r) (Gallay and Klink, 1986).

$$\eta = \frac{V_s}{2V_r} \qquad [4.4]$$

Due to the relationship between the power of the output signal (P_o) to η, Q, and the input power (P_i), reducing the resonator to match the tissue size as closely as possible or increasing the filling factor increases the signal (Gallay and Klink, 1986).

$$P_o \propto \eta Q P_i \qquad [4.5]$$

The SNR depends indirectly on the filling factor; however, SNR is only partly dependent on the hardware; the more malleable parameters of the imaging sequence directly influence SNR. For a specific specimen size and power input, as resolution increases, the voxel size (pixel width (Δx) x pixel height (Δy) x slice thickness (Δz)) of the image decreases as well as the signal per voxel. Obtaining

multiple images and averaging them is one way to increase the SNR; however, it increases scan time. Reducing the RF coil radius (r) focuses the RF signal and increases the SNR (Doty et al., 2007).

$$SNR \propto \frac{\Delta x \Delta y \Delta z * B_0 * N}{r * \sqrt{BW/DIMM1}} \quad [4.6]$$

The electromagnetic force of the primary static magnet (B_0) is generally fixed, whereas the radius of the RF coil is semipermanent and the number of averages (N), the bandwidth (BW), and the width of the image ($DIMM1$) are adjustable. Experimentally, SNR is determined by calculating the mean signal (S) of a region-of-interest (ROI) divided by the standard deviation of an ROI in background noise (SD_n) or outside of the tissue region (Constantinides et al., 1997).

$$SNR = \frac{S}{SD_n} \quad [4.7]$$

For separating the annulus from the nucleus, the key factor is the contrast-to-noise ratio (CNR) as it defines the ability to distinguish one tissue from another.

$$CNR = SNR_{Tissue\ A} - SNR_{Tissue\ B} \quad [4.8]$$

The final key parameter in MRI is the scan time. Scan time lengthens with increasing numbers of pulse sequences and iterations for averaging to gain SNR.

Scan time affects the budget of a study as MRI usage fees are often costly. Subject welfare is also a consideration as rats anesthetized greater than 1 hour are prone to fatalities as breathing and heart rates become more sporadic. The SNR is balanced between the scan time and the intended information for the study.

To establish a baseline for the distraction system under development, a commercially made 10 mm ID quadrature birdcage RF coil (Model 10 mm ID Quadrature RF Coil, m2m Imaging Corp., Cleveland, OH) was used in a 7 Tesla MRI scanner (Model BioSpec 70/30 Bruker Inc., Billerica, MA). This coil fits tightly around tails of rats under 300 g, maximizing the filling factor, and despite the inhomogeneity shown in Figure 4.2, has an SNR of 182 over 16 mm of the coil length. The *ex vivo* rat-tail annulus SNR of 19.88 and nucleus SNR of 9.44 yield a CNR of 10.44, providing images suitable for separating the nucleus from the annulus (Figure 4.3). Unfortunately, the 10 mm ID RF coil was inadequate for the distraction setup as the rings were 26.38 mm in diameter.

The next larger available RF coil was a commercial 35 mm ID quadrature RF coil (Model 35 mm Quadrature RF Coil, RAPID MR International, LLC., Columbus, OH). However, this coil produced poor images compared to the commercial 10 mm ID RF coil, because the commercial 10 mm ID RF coil had a filling factor closer to 0.5, while the commercial 35 mm ID RF coil's filling factor was 0.08 with a rat-tail. The SNR of the 35 mm RF coil calculated using a 10 ml saline phantom was 21 with an MSME pulse sequence of 40 x 40 mm FOV, ST 1 mm, TR 1000 ms, and TE 15 ms (Figure 4.4a). To compensate for the low signal

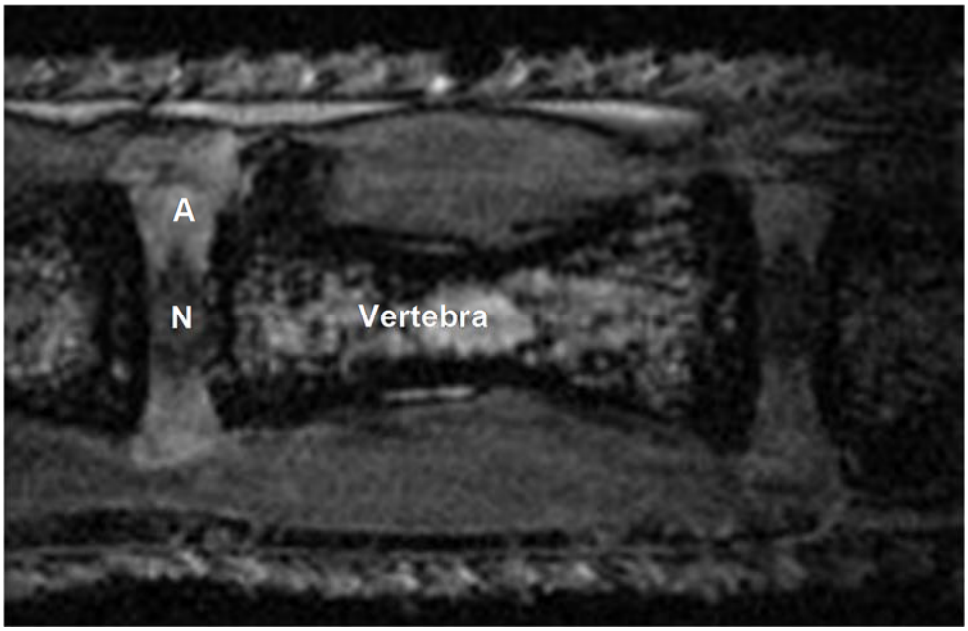

Figure 4.3: With an annulus SNR of 19.9 and nucleus SNR of 9.4, the sagittal T1 MRI scan of an *ex vivo* rat-tail with the 10 mm commercial RF coil provides clear definition between the nuclear tissue (N) and the annulus (A) and is possible with live animals. MP RAGE 15 x 10 mm FOV, 0.07 x 0.09 mm/voxel, ST 0.25 mm, TR 3000, TE 4, Inversion Time 1100ms, 1 Average.

quality of the bigger coil, the slice thickness was increased to 0.4 mm, the voxel size from 0.07 x 0.09 mm/pixel to 0.1 x 0.1 mm/pixel, the field of view reduced from 10 x 15 mm to 10 x 10 mm, and number of averages increased. With an annulus SNR of 13, nucleus SNR of 7 and CNR between the annulus, and nucleus of 6, IVD images of an *in vitro* rat-tail using the larger coil did not provide definable regions to segment images for 3D analysis (Figure 4.4b).

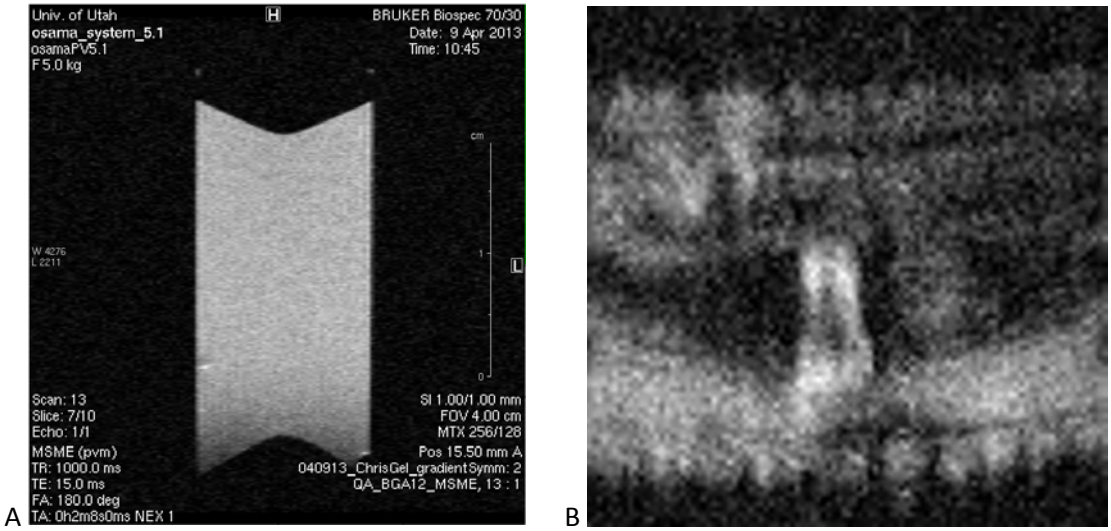

Figure 4.4: (A) Characterizing the 35 mm RF coil with a saline phantom and a filling factor of 0.08 yielded an SNR of 21. (B) Using the 35 mm RF coil, the IVD in a sagittal T1 MRI scan of a rat-tail lacks definition with an annulus SNR of 13, a nucleus SNR of 7 and a CNR of 6.4. MP RAGE, 10 x 10 mm FOV, 0.1 x 0.1 mm/voxel, ST 0.4 mm, TR 3000, TE 4, Inversion Time 1100 ms, 1 Average.

4.3. MRI Requirements

Current imaging using radiograph is done quickly and inexpensively; however, it lacks soft tissue differentiation between the nucleus and annulus. With the right RF coil and protocols, MRI can separate the two IVD structures. Scan time and the resulting image costs must be balanced with image requirements. The MRI system must allow for the implanted rings in the tail. To distinguish the annulus from the nucleus, the target CNR between the annulus and nucleus for the T1-weighted image is 10 with a minimum of 8 for an *ex vivo* rat-tail.

Assuming the center sagittal slice of the IVD is 4.5 mm x 1.0 mm, the minimum voxel size needed to represent the 0.25 mm radius curvature of an IVD

nucleus is 0.1 mm x 0.1mm. For a 4.5 mm diameter IVD, the minimum slice thickness to segment the T1-weighted stack for 3D rendering and volume measurements is one-tenth the diameter or 0.45 mm. The image requirements must be balanced with budget and animal welfare considerations and limit the scan time for each animal to 30 minutes total for the T1-weighted scan and the T2-weighted map.

In addition, the MRI setup must take into account the health of the anesthetized animals while being imaged. Animals require critical function monitoring, breath support, thermoregulation, and during MRI scans, anesthesia administration. Monitoring vital signs while animals are in an MRI is done by one or any combination of four methods: EEG, tail blood pressure, heart rate, and/or respiratory rate. For rat imaging, the most efficient technique is managing the respiratory rate using a pressure sensor under the rat's abdomen to measure changes in pressure resulting from inspiration and exhalation. Pressure measurements transmitted outside of the MRI chamber are converted into a continuous plot and calculate respiratory rates based on the spikes in the plot. The system must monitor at least one of the animal's vital functions to maintain homeostasis.

Due to the high metabolism of rodents and the large surface area to volume ratio, rats rapidly lose heat especially under anesthesia. To maintain thermal homeostasis, a heat source is required. The heat source could either be a recirculating water heat pad as was used in surgeries or a feedback-controlled convection heater. In convection heating, a probe is placed on or near the animal

to monitor thermal fluctuations and adjust the heating accordingly. Temperature measurements, like the respiratory rate are displayed with the respiratory rate.

4.4. Loop-gap Single-turn Solenoids

Commercial body RF coils are often designed as birdcages, surrounding the subject with strips of conducting material lining the coil main axis. Because the coil is made of strips rather than a single solid piece of conducting material, the RF field is naturally inhomogeneous, as shown in Figure 4.2, causing transmission distortions and decreased signal reception (Fan et al., 2006). With multichannel shimming, moderate variances in the field are relatively homogeneous; however, it becomes less homogeneous as the frequency increases (Ibrahim et al., 2001). As was the case with the 35 mm coil, body coils are often larger than the subject; however, creating customized bird-cage body coils require difficult to obtain infinitely small capacitors.

The coupled loop-gap single-turn solenoid uses a single piece of conducting material to form the coil's bore increasing homogeneity and signal reception (Hornak et al., 1986). The continuous coverage of a solid conductive material solenoid typically has a Q value of greater than 400 and highly efficient RF transmittal/reception (Hornak et al., 1986). Their one-piece solenoid construction requires a higher capacitance than a bird cage coil to obtain the same resonance frequency and therefore is easier to construct. RF variation within the resonator of a coupled loop-gap solenoid is 10%-30% over the central 70% of the resonator volume (Hornak et al., 1986; Hornak et al., 1987). One

main advantage other coils have over the coupled loop-gap single-turn solenoid is subject position. MRI requires an RF pulse perpendicular to the axis of the main magnet to initiate the imaging sequence. Loop-gap single-turn solenoids create the magnetic field parallel to their primary axis and therefore must be positioned perpendicular to the bore of the main magnet to begin the imaging sequence. Birdcage and saddle coils create the magnetic field perpendicular to their primary axis; therefore, they are placed parallel to the bore of the main magnetic field, making subject placement and removal easier.

In the loop-gap single-turn resonator, a coupling loop inductively connects the resonator to the external MRI systems, forming an impedance matching transformer. Varying the distance between the coupling loop and resonator improves transformer matching, which changes with the filling factor (Figure 4.5). The coupling arrangement can have significant losses in the coils' magnetic field

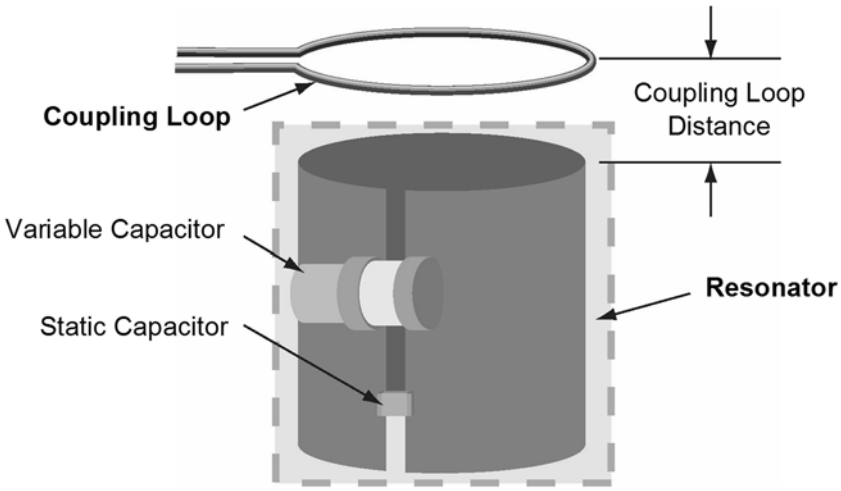

Figure 4.5: The resonator transmits and receives the RF signal through the electromagnetic force of the solid conductor. The coupling loop provides the interface through induction.

and SNR (Hornak et al., 1986). In the stainless-steel coaxial line loop-gap coils are made of, there is 3dB of signal attenuation in 500 mm of cable (Gallay and Klink, 1986). In small animal imaging, the problems associated with the coupled loop-gap single-turn solenoid at times are outweighed by the increased SNR and homogeneous RF field of the single-turn solenoid.

To create a single-turn solenoid for the distraction system, first, the required size was determined. For the distraction system, the width of the resonator was dictated by the Psf rings, the syringe chosen for them to slide in, and length of tail to image with a single sequence. To image the target distraction disc and an adjacent disc, the field-of-view (FOV) must be at least 11 mm x 4 mm. The syringe chosen for the rings to slide in and the resonator to wrap around had an outer diameter of 26.38 mm. Copper foil, 0.05 mm thick x 39.79 mm wide with an adhesive paper backing formed the single-turn solenoid. A 30 mm wide foil provided 63% more coverage than the required 11 mm FOV, allowing for the intensity fall-off at the ends of RF coils yet still allowing room for the perpendicular orientation in the main magnet. The paper backing was left in place for resonator removal from the construction syringe and adjustment of the coupling distance. This size coil yields inductance (L) as measured in Henry's (H) or ($kg \cdot m^2)/(s^2 \cdot A^2$) in terms of the solenoid radius (r), length (Z) and the permeability constant (μ)

$$L = \mu \pi r^2 / Z \qquad [4.9]$$

With the solenoid dimensions for this study of r=14.73 mm and Z= 29.79 mm with $\mu = 4\pi$E-7 N/A^2, L is equal to 2.856E-8 H. For maximum efficiency, the resonance frequency of the solenoid is matched to the resonance frequency of the main magnet. The 7T MRI scanner at the University of Utah Small Animal Imaging Facility has a resonance frequency of 300.3 MHz. The desired resonance frequency (υ) is dependent on L and capacitance (C).

$$\upsilon = \frac{1}{2\pi\sqrt{LC}} \qquad [4.10]$$

For a υ of 300.3 MHz, the required C is calculated as 9.84 pF for the combination of a variable capacitor to fine-tune the resonance frequency of the coil and static capacitors. Capacitance can be created with multiple capacitors along the gap to increase homogeneity in larger coils. For this solenoid, a static 8.2 pF ±5% capacitor (Model ATC 82RJ 100B 100JWN 200W VDC, American Technical Ceramics, Huntington Station, NY) was combined with a variable 1-16 pF capacitor (Model NMAP15HV-E, Voltronics Corp., Salisbury, MD). The single-turn coupling coil was fabricated from 18 AWG copper magnet wire wrapped around the solenoid syringe, crossed, and soldered to a coaxial cable that was connected to the MRI capture system (Model Paravision, Bruker Inc., Billerica, MA) (Figure 4.6). The resonator and coupling coil were matched using a network analyzer (Model ENA Series Network Analyzer, Agilent Technologies, Santa Clara, CA), a 3 ml syringe filled with 0.09 % saline to approximate a rat-tail with

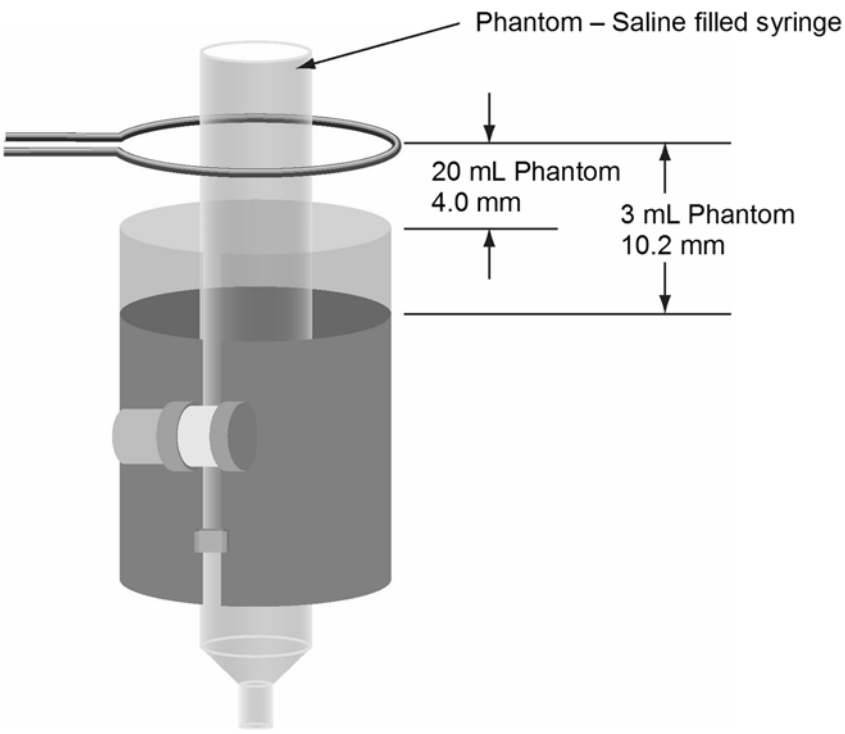

Figure 4.6: Solenoids are characterized with saline or other homogenous solutions. As the sample volume increases, the coupling loop distance reduces to maintain coil matching. The quality factor is determined using a phantom with a filling factor close to 0.5.

filling factor, 0.059, and a 20 ml saline filled syringe with a filling factor of 0.25 was used to determine the quality factor.

Matching of the coupling coil to the resonator consisted of changing the longitudinal distance between them until the signal was maximized. Adjusting the variable capacitor altered the resonance frequency. For a resonance frequency of 300.3 MHz with a signal peak of 55.02 dB using the 20 ml syringe with a 0.26 filling factor, the full width bandwidth at half of resonance peak was 0.6 MHz and by equation 4.3, the quality factor was 500.5 (Figure 4.7).

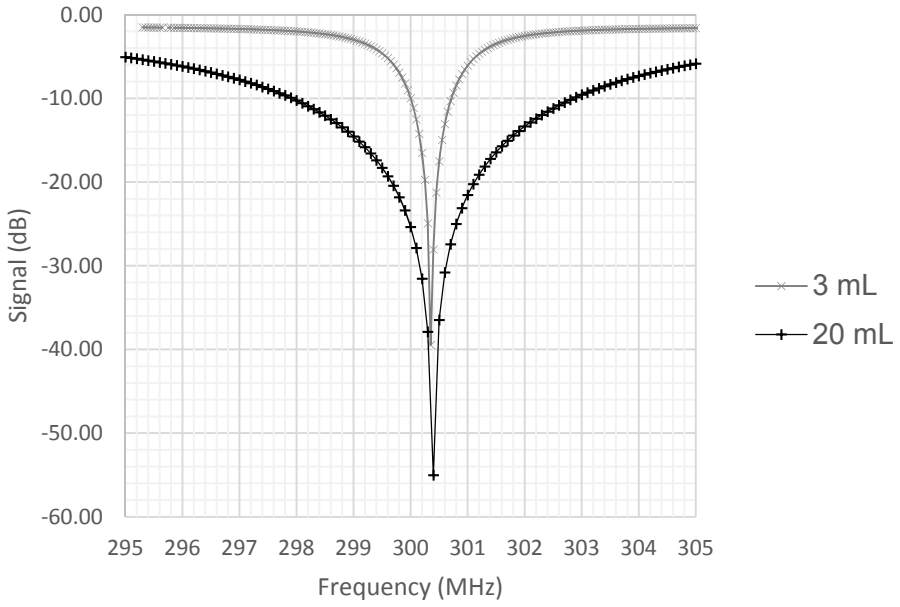

Figure 4.7: Matching using the network analyzer illustrated the difference the filling factor makes as the increased sample volume resulted in more signal than the smaller sample volume.

The homogeneity test shown in Figure 4.8 used the described custom coil in the 7T MRI at the University of Utah with an MPRAGE T1 scanning sequence (FOV 40 mm x 40 mm, ST 1 mm, TR 1000, TE 15, AVG 1, ETL 1). Tests conducted directly after construction of the coil combined with tests conducted after hundreds of hours of service resulted in an RF field variability of 16.1 ±4.0% for over 70% of the length of the coil or 20.9 mm of the 29.8 mm long coil. Tests conducted directly after fabrication of the coil had 14.0 ±0.7% RF field variability.

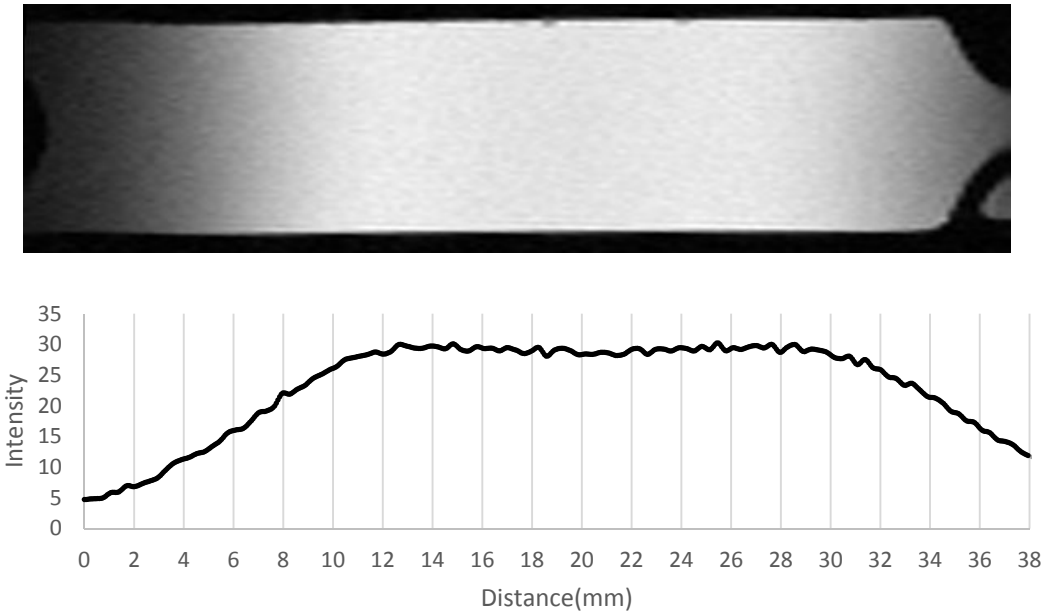

Figure 4.8: A homogeneity test of the loop-gap single-turn solenoid showed a “sweet spot” or flat signal response between 10 mm and 31 mm which is the optimal subject placement for imaging with this RF coil. T2 MSME 40 x 40 mm FOV, 0.31 x 0.16 mm/voxel, ST 1.0 mm, TR 1000, TE 15, 1 Average.

4.5. Imaging Bed

Using the single-turn solenoid has two challenges. First, the coil must be mounted perpendicular in the coil. Second, the coil must be adjustable. In animal studies, there are variations in the physical size of animals. As was discussed earlier, changing subject volumes in the single-turn solenoid alters the loop coupling – resonator matching. Adjusting the matching as needed by rat-tail size is necessary to achieve optimal imaging.

An imaging bed was created from ABS using a 3D printer, taking into account animal physiology, imaging mechanisms, and study demands. The bed was designed to accommodate the 12 cm bore size of the 7T MRI with the

perpendicular solenoid containing a rat-tail (Figure 4.9). Solenoid match adjustments were made by modifying the position of the coupling loop and resonator along a piece of a 60 ml syringe shaped to accommodate a rat-tail. The syringe pivoted to ease animal positioning.

An anesthesia machine (Model Ohmeda Isotec 5, BOC Healthcare, West Yorkshire, England) administered isofluorane through a rat nose adapter that fed the animal anesthetic and oxygen while removing the excess anesthetic with a second line (Figure 4.10). Moving the adapter along the bed allowed for a wide range of animal sizes.

Heating from an MR-compatible convection heater (Model Heater System for Small Animals, SA Instruments, Stony Brook, NY) was applied through a central air heating system of ducts within the bed. After being inserted into the

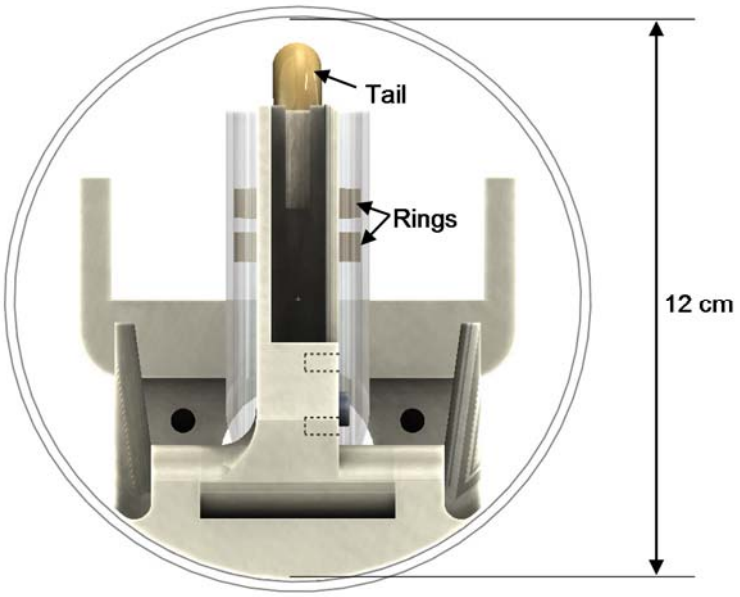

Figure 4.9: The MRI bore volume was maximized by designing the bed with a computer aided design program and creating it with a 3D printer.

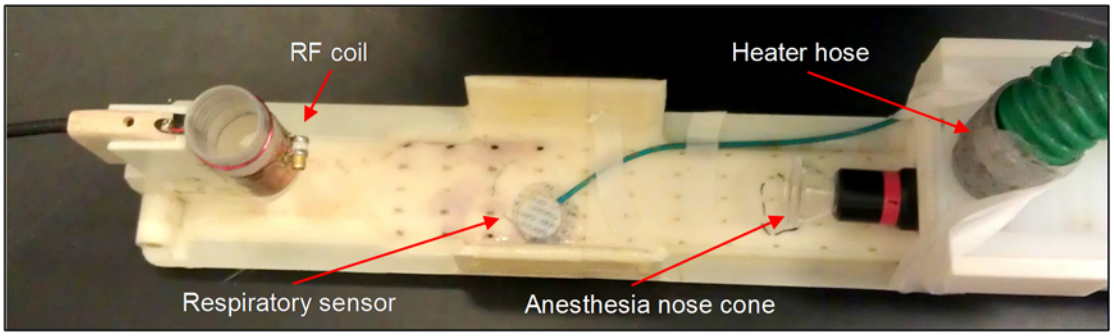

Figure 4.10: The respiratory sensor and nose cone are moved according to the animal's dimensions.

vents, heated air first exited vents passing air over the head before sending air through the bed base vents along the body of the animal (Figure 4.11). The base ducts were open at the bottom to reduce over-heating from pressure buildup of the heated air. A thermal probe near the head monitored thermal fluctuations.

Respiratory rates were measured with a pressure sensor from an image gating system (Model Multi-animal Monitoring and Gating System SA Instruments, Stony Brook, NY) placed under the abdomen and 25 mm tall sides constrained the animal with room for natural limb repose.

A custom machined plate mounted a 47.0 cm ultra-high molecular weight polyethylene (UHMWPE) bridge to the MRI slide on one side and the described bed on the other (Figure 4.12).

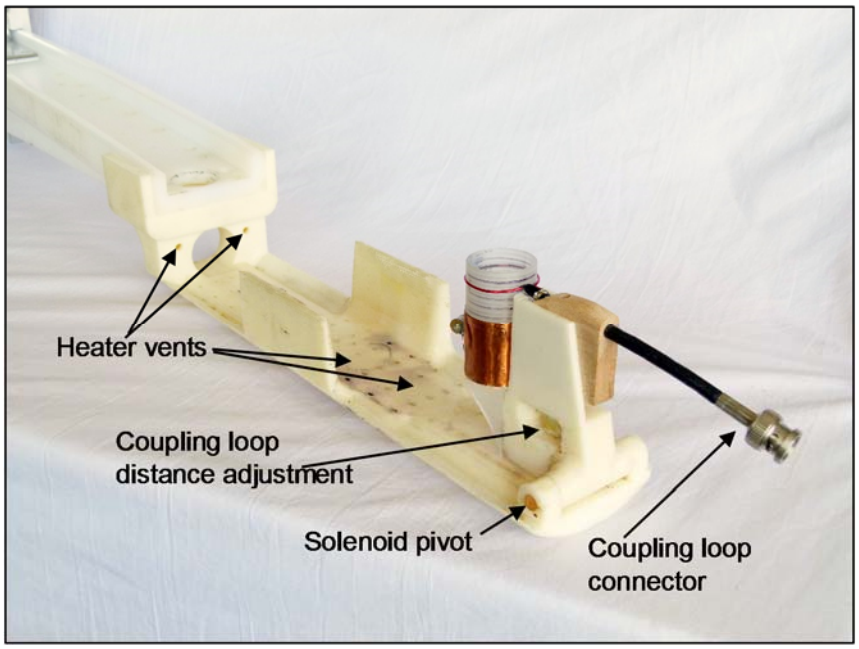

Figure 4.11: The MRI bed's internally printed ducting spread heat along the animal's body, while the sides contained the thorax.

Figure 4.12: The mounting plate was machined out of a block of aluminum to form a rigid interface between the bridge and the slide of the MRI structure.

4.6. MRI Validation

Repeated daily stresses and minor injuries of the soft tissues between the vertebrae, known as the intervertebral discs, can accumulate over time, causing disc degeneration. Animal studies have often been used for *in vivo* spine research, with rat-tails being used extensively because of their accessibility. Many investigators have used an Ilizarov-type device to compress or to distract the intervertebral disc. Unfortunately, these devices are typically fabricated from various metals, which create artifacts or projectiles with MRI the modality often used for human diagnostics of intervertebral disc problems.

The loop-gap single-turn solenoid provided images that differentiated the nucleus from the annulus with segmentable resolution. The SNR of the 30 mm loop-gap single-turn RF coil calculated using a 10 mL saline phantom was 68 (Figure 4.13). With an annulus SNR of 15.3, a nucleus SNR of 7.6, and a CNR of 7.7, the tissues of the IVD were diferentiable. Installed carbon fiber rods and the attached rings had minimal impact on visualizing and quantifying IVD on either side of implanted vertebrae despite susceptibility artifacts (Figure 4.14). The artifacts in the center of the vertebra resulted from the distorted magnetic field generated by the substantial change between the carbon fiber and tissue's susceptibility to magnetization. The voxel size of the T1-weighted images was 0.1 x 0.1 mm with a slice thickness of 0.4 mm, providing adequate resolution for 3D rendering segmentation. T1-weighted scans were conducted in 21 minutes and T2-weighted scans were obtained in 5 minutes. Strictly for visualization, MRI images were resampled from the orginal 100 x 150 pixels to 1003 x 1595 pixels

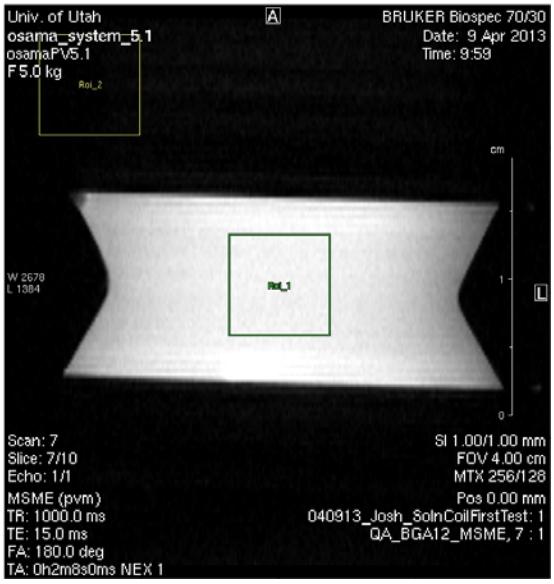

Figure 4.13: The 10 mL phantom in the 30 mm loop-gap single-turn RF coil had an SNR of 68 with a filling factor of 0.11. MSME pulse sequence with 40 x 40 mm FOV, ST 1 mm, TR 1000, TE 15.

using a freeware image analysis program (Model ImageJ, National Institutes of Health, Bethseda, MD) with bicubic interpolation.

The MRI bed's animal life-sustaining features were tested through imaging 40 rats, four times over 6 months, for 30 minutes at a time. All animals were sedated using a separate anesthesia chamber and transferred to the MRI bed for imaging. There were no complications resulting from the bed or the life-sustaining features: respiratory monitoring, heating, or anesthesia.

To validate tissue identification, animals were imaged with the MRI system and within 4 days, they were euthanized and the tails were harvested. The skin was removed and selected sections placed in refrigerated 10% buffered formalin at 4 C overnight. After removing some of the tendons, specimens were

Figure 4.14: A sagittal T1 MRI of a rat C7-8 disc (A) and the C6-7 disc (B) shows the annulus and nucleus of both discs. The blackened marks on the center of the vertebrae are susceptibility artifacts. MP RAGE 15 x 10 mm FOV, 0.1 x 0.1 mm/voxel, ST 0.4 mm, TR 3000, TE 4, Inversion Time 1100 ms, 1 Average.

decalcified with a formic acid solution (Model Formical-2000, Decal Chemical Corp., Suffern, NY) and kept at 4 C. After 5 days of daily refreshing the decalcification solution, no calcium ions were detected with an ammonium oxalate turbidity test and the specimens were rinsed briefly in deionized water (Sheehan and Hrapchak, 1987). The decalcified specimes were embedded with low-temperature paraffin and stored at 4 C. The sections were cut into 5 μm slices with a microtome (Model Cut 4060, Olympus America Inc., Center Valley, PA) then the slices were air dried onto glass slides (Model Superfrost Plus,

Fisher Scientific International, Inc., Pittsburgh, PA), after which they were incubated at 37 C overnight, then stored at 4 C. For MRI and histology correlation, the sections were stained with hematoxylin and eosin (H&E) (Figure 4.15).

MRI stacks were converted into TIFF images with a freeware image analysis program (ImageJ, National Institutes of Health, Bethseda, MD) and imported into a 3D image analysis software (Model Amira 5.50, FEI Visualization Sciences Group, Hillsboro, OR) to create 3D volume renderings. The nucleus and annulus of the IVD were selected on each slice based on the correlating histological information using manual techniques (Figure 4.16).

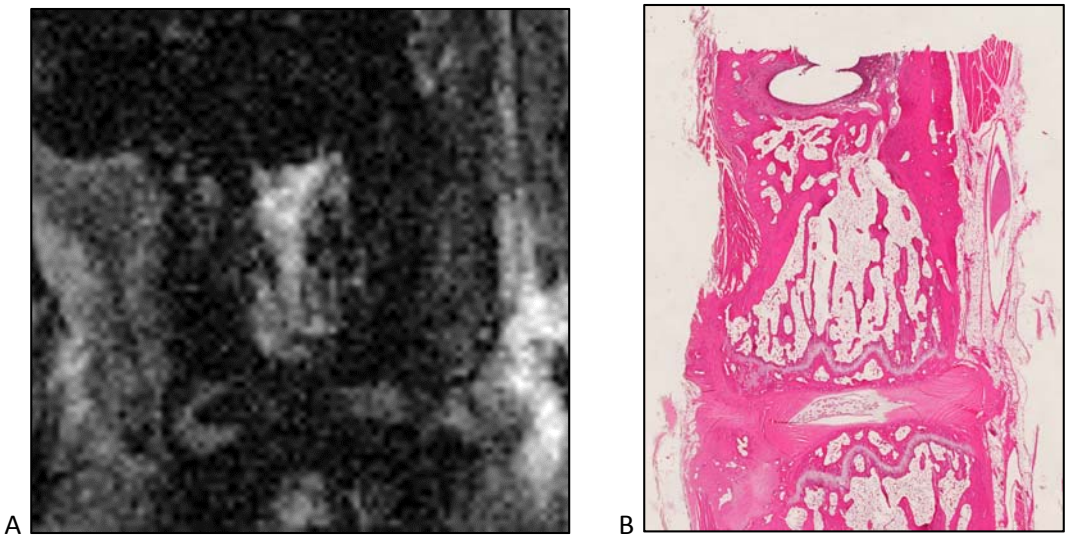

Figure 4.15: While a T1-weighted MRI slice (A) and hematoxylin and eosin stained histological slide (B) could not be matched up exactly due to variations in slice position, there was substantial anatomical correlation between them. MP RAGE 15 x 10 mm FOV, 0.1 x 0.1 mm/voxel, ST 0.4 mm, TR 3000, TE 4, Inversion Time 1100ms, 1 Average.

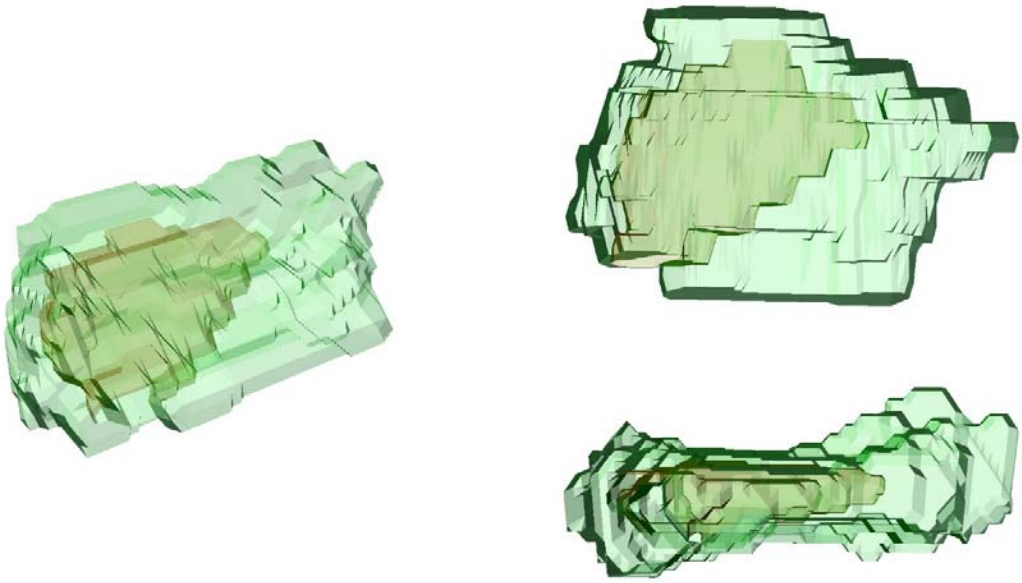

Figure 4.16: The MRI images with the custom coil were suitable for selecting regions on each slice of the MRI scans(segmenting) to create rough 3D renderings of both the annulus (transparent green) and nucleus (brown).

CHAPTER 5

CONCLUSION

5.1. Conclusion

This study met the goals of designing, fabricating, and testing a distraction device for IVD decompression studies using a rat-tail model. Using carbon fiber rods and Psf rings to create the Ilizarov-type device, we have minimized MRI artifacts and eliminated them from the regions of interest, the IVD. The carbon fiber rod and Psf ring construct has been structurally validated and *in vivo* tested with rats. Modified traditional Ilizarov-type implantation eliminated vascular disruption as evidenced by the lack of hemorrhaging and, it is believed, reduced neural damage; however, that could not be determined.

A custom pressure sensor feedback-controlled pneumatic system provided the distractive force by inflating a bladder inserted between the Psf rings. Distractive forces at frequencies within human clinical loading practices applied to a rat are possible. The distraction cycle is programmable and the system individually adjusts to multiple animals simultaneously. Un-anesthetized animals undergoing distraction treatments can be monitored for behavior reactions while they move freely about their enclosure. The system only attaches to the animal

during treatments, allowing complete freedom when not being treated and uninhibited MRI sessions.

A loop-gap single-turn RF coil seated in a bed accommodated the solenoid's perpendicular orientation to the primary axis of the main magnet and captured T1-weighted MR images with voxel sizes and SNR suitable for 3D measurements. The MR images were validated by postmortem histological comparison. The bed maintained animal homeostasis.

5.2. Discussion

This study met the goals of designing, fabricating, and testing a distraction system that minimized MRI artifacts and allowed the system to be used with *in vivo* MRI studies; however, there are ways it could be improved. The periprosthetic tissues of 38 of the animals became inflamed and subsequently infected, requiring treatment with antibiotics and resulted in eight deaths. The pathology implicates the carbon fiber rods. The carbon fiber rods used were made with 15% epoxy resin and 85% carbon fiber. A study implanting rods with a varying amounts of epoxy resin content may show that an increased resin content will encapsulate the carbon fiber more fully and reduce inflammation. Applying cyanoacrylate adhesive or epoxy to the end of the carbon fiber rod post-sharpening may also encapsulate the fibers and further reduce inflammation.

While this distraction device was designed around using a circular shaped bladder, an oval bladder could reduce the overall width of the rings and increase the tail range of motion. The four-fold cost increase for PEEK over polysulfone or

creation of carbon fiber molds to fabricate the rings may be justified with structural analysis to reduce their overall size for mobility and MR reasons discussed in Chapter 4.

The surgery developed is a modified version of those used in other studies (Akyuz et al., 2006; Korecki et al., 2008; Lai et al., 2007; Maclean et al., 2004; MacLean et al., 2003; MacLean et al., 2008; Stinnett-Donnelly et al., 2007; Wuertz et al., 2009). While damage to the vasculature can be observed as hemorrhaging, neural damage cannot be readily diagnosed. It is possible and likely that despite measures taken to avoid neural damage, some nerve fibers could have been injured. As mechanoreceptors, pain, and other signals travel along the fibers, a study examining the effects of nerve damage on degeneration and regeneration are of interest, especially since the position and degree of innervation is associated with pathologies (Fields et al., 2014).

While meeting the goals of the study, the distraction system could be improved for ease of use and increased control. Increasing the sample rate from 1.5 kHz would improve the responsiveness of the system and the ability of the system to track the signal. Increasing the sample rate would require changing the hardware of the controller from the NI cDAQ system, which is limited by DAQ to computer communication, to an embedded system. Replacing the manifold/pressure vessel system by a pressure vessel with the manifold built in to it would also improve the responsiveness and reduce system vibrations. Currently, the pressure in the manifold varies with each valve movement. The pressure vessels provide a large reservoir to minimize solenoid pneumatic valve

fluctuations' impact on the system. With the pressure vessels offset from the valves through the manifold, pressure fluctuations occur in the cavity of the manifold and reduce the impact of the pressure vessels.

Latex bladder manufacturing was manually conducted using a set protocol; however, variations in the elastic properties of the bladders expose fabrication deficits. Due to labor, equipment, and environmental limitations, a maximum of four bladders could be made in a day. With each bladder and over time, the solution thickens, altering the coating properties. Manual fabrication introduces further variability. Mechanizing the system and increasing throughput with more mandrels or more focused labor would reduce many of the variables and improve bladder consistency.

Reducing the error between bladder pressure and the force exerted on the ring would need to be studied to determine the cause of the error. Investigations into dry lubricants, graphite, and Teflon did not show a change in the loading behavior.

MRI images using the loop-gap single-turn RF coil could be improved with further development. The RF used in the study had a single conductor. Adding more conducting coils and a shield around them would improve the quality factor of the coil and the SNR of the images.

REFERENCES

Adams, M.A., Bogduk, N., Burton, K., al., e., 2002. The Biomechanics of Back Pain. Churchill Livingstone, Edinburgh, UK.

Adams, M.A.P., Roughley, P.J.P., 2006. What is Intervertebral Disc Degeneration, and What Causes It? [Review]. Spine 31, 2151-2161.

Akyuz, E., Braun, J.T., Brown, N.A.T., Bachus, K.N., 2006. Static Versus Dynamic Loading in the Mechanical Modulation of Vertebral Growth. Spine 31, E952-E958.

Ali, M.S., French, T.A., Hastings, G.W., Rae, T., Rushton, N., Ross, E.R., Wynn-Jones, C.H., 1990. Carbon Fibre Composite Bone Plates. J Bone Joint Surg Br 72-B, 586-591.

An, H.S., Thonar, E., Masuda, K., 2003. Biological repair of intervertebral disc. Spine 28, S86-S92.

Barbir, A., Godburn, K.E., Michalek, A.J., Lai, A., Monsey, R.D., Iatridis, J.C., 2011. Effects of torsion on intervertebral disc gene expression and biomechanics, using a rat tail model. Spine 36, 607-614.

Beckstein, J.C.S., S.; Schaer, T. P.; Vresilovic, E. J. ; Elliott, D. M., 2008. Comparison of animal discs used in disc research to human lumbar disc: axial compression mechanics and glycosaminoglycan content. Spine 33, E166-E173.

Bibby, S.R., Jones, D.A., Ripley, R.M., Urban, J.P., 2005. Metabolism of the intervertebral disc: effects of low levels of oxygen, glucose, and pH on rates of energy metabolism of bovine nucleus pulposus cells. Spine 30, 487-496.

Bushberg, J.T., 2012. The essential physics of medical imaging, 3rd ed. Wolters Kluwer Health/Lippincott Williams & Wilkins, Philadelphia.

Callister, W.D., Rethwisch, D.G., 2008. Fundamentals of materials science and engineering : an integrated approach, 3rd ed. John Wiley & Sons, Hoboken, NJ.

Cassidy, J.J., Hiltner, A., Baer, E., 1989. Hierarchical structure of the intervertebral disc. Connect Tissue Res 23, 75-88.

Constantinides, C.D., Atalar, E., McVeigh, E., Year Signal-to-noise measurements in magnitude images from NMR phased arrays. In Engineering in Medicine and Biology Society, 1997. Proceedings of the 19th Annual International Conference of the IEEE.

Dickinson, B.L., 1989. UDEL polysulfone for medical applications. Journal of biomaterials applications 3, 605-634.

Doty, F.D., Entzminger, G., Kulkarni, J., Pamarthy, K., Staab, J.P., 2007. Radio frequency coil technology for small-animal MRI. NMR in biomedicine 20, 304-325.

Elliott, D.M., Sarver, J.J., 2004. Young Investigator Award Winner: Validation of the Mouse and Rat Disc as Mechanical Models of the Human Lumbar Disc. Spine 29, 713-722.

Fan, X., Markiewicz, E.J., Zamora, M., Karczmar, G.S., Roman, B.B., 2006. Comparison and evaluation of mouse cardiac MRI acquired with open birdcage, single loop surface and volume birdcage coils. Physics in medicine and biology 51, N451.

Fields, A.J., Liebenberg, E.C., Lotz, J.C., 2014. Innervation of pathologies in the lumbar vertebral end plate and intervertebral disc. The Spine Journal 14, 513-521.

Fritz, J.M., Thackeray, A., Childs, J.D., Brennan, G.P., 2010. A randomized clinical trial of the effectiveness of mechanical traction for sub-groups of patients with low back pain: study methods and rationale. BMC Musculoskeletal Disorders 11, 1-10.

Fujiwara, A., Lim, T.H., An, H.S., Tanaka, N., Jeon, C.H., Andersson, G.B., Haughton, V.M., 2000. The effect of disc degeneration and facet joint osteoarthritis on the segmental flexibility of the lumbar spine. Spine 25, 3036-3044.

Gallay, R., Klink, J.J.v.d., 1986. Resonator and coupling structure for spin-echo ESR. Journal of Physics E: Scientific Instruments 19, 226.

Gay, R.E., Bronfort, G., Evans, R.L., 2005. Distraction Manipulation of the Lumbar Spine- A Review of the Literature. Journal of manipulative and physiological therapeutics 28, 266-273.

Gay, R.E., Ilharreborde, B., Zhao, K.D., Berglund, L.J., Bronfort, G., An, K.N., 2008. Stress in lumbar intervertebral discs during distraction: a cadaveric study. The spine journal : official journal of the North American Spine Society 8, 982-990.

Geiringer, S.R., deLateur, B.J., 1990. Physiatric therapeutics. 3. Traction, manipulation, and massage. Archives of physical medicine and rehabilitation 71, S264-266.

Giampietro, P.F., Dunwoodie, S.L., Kusumi, K., Pourquié, O., Tassy, O., Offiah, A.C., Cornier, A.S., Alman, B.A., Blank, R.D., Raggio, C.L., Glurich, I., Turnpenny, P.D., 2009. Progress in the Understanding of the Genetic Etiology of Vertebral Segmentation Disorders in Humans. Annals of the New York Academy of Sciences 1151, 38-67.

Goh, S., Price, R.I., Leedman, P.J., Singer, K.P., 1999. The relative influence of vertebral body and intervertebral disc shape on thoracic kyphosis. Clinical biomechanics (Bristol, Avon) 14, 439-448.

Guehring, T., Omlor, G.W., Lorenz, H., Engelleiter, K., Richter, W., Carstens, C., Kroeber, M., 2006. Disc Distraction Shows Evidence of Regenerative Potential in Degenerated Intervertebral Discs as Evaluated by Protein Expression, Magnetic Resonance Imaging, and Messenger Ribonucleic Acid Expression Analysis. Spine 31, 1638-1665.

Guyton, A.C., Hall, J.E., 2006. Textbook of medical physiology, 11th ed. Elsevier Saunders, Philadelphia.

Henninger, H.B., Barg, A., Anderson, A.E., Bachus, K.N., Tashjian, R.Z., Burks, R.T., 2012. Effect of deltoid tension and humeral version in reverse total shoulder arthroplasty: a biomechanical study. Journal of shoulder and elbow surgery / American Shoulder and Elbow Surgeons ... [et al.] 21, 483-490.

Hibbeler, R.C., 2008. Mechanics of materials, 7th ed. Pearson/Prentice Hall, Upper Saddle River, N.J.

Hickey, D.S., Hukins, D.W., 1980. X-ray diffraction studies of the arrangement of collagenous fibres in human fetal intervertebral disc. J Anat 131, 81-90.

Hornak, J.P., Ceckler, T.L., Bryant, R.G., 1986. Phosphorus-31 NMR spectroscopy using a loop-gap resonator. Journal of Magnetic Resonance (1969) 68, 319-322.

Hornak, J.P., Szumowski, J., Bryant, R.G., 1987. Elementary single turn solenoids used as the transmitter and receiver in magnetic resonance imaging. Magnetic resonance imaging 5, 233-237.

Howard, C.B., Tayton, K.J., Gibbs, A., 1985. The response of human tissues to carbon reinforced epoxy resin. J Bone Joint Surg Br 67, 656-658.

Hristova, G.I., Jarzem, P., Ouellet, J.A., Roughley, P.J., Epure, L.M., Antoniou, J., Mwale, F., 2011. Calcification in human intervertebral disc degeneration and

scoliosis. Journal of orthopaedic research : official publication of the Orthopaedic Research Society 29, 1888-1895.

Ibrahim, T.S., Lee, R., Baertlein, B.A., Robitaille, P.-M.L., 2001. B 1 field homogeneity and SAR calculations for the birdcage coil. Physics in medicine and biology 46, 609.

Jaskwhich, D., Ali, R.M., Patel, T.C., Green, D.W., 2000. Congenital scoliosis. Current opinion in pediatrics 12, 61-66.

Judovich, B., Nobel, G.R., 1957. Traction therapy, a study of resistance forces: Preliminary report on a new method of lumbar traction. The American Journal of Surgery 93, 108-114.

Judovich, B.D., 1955. Lumbar traction therapy; elimination of physical factors that prevent lumbar stretch. Journal of the American Medical Association 159, 549-550.

Korecki, C.L., MacLean, J.J., Iatridis, J.C., 2008. Dynamic Compression Effects on Intervertebral Disc

Mechanics and Biology. Spine 33, 1403-1409.

Kroeber, M., Unglaub, F., Guehring, T., Nerlich, A., Hadi, T., Lotz, J.C., Carstens, C., 2005. Effects of Controlled Dynamic Disc Distraction on Degenerated Intervertebral Discs: An in Vivo Study on the Rabbit Lumbar Spine Model. Spine 30, 181-187.

Lai, A., Chow, D.H., Siu, W.S., Holmes, A.D., Tang, F.H., 2007. Reliability of radiographic intervertebral disc height measurement for in vivo rat-tail model. Medical engineering & physics 29, 814-819.

Lai, A., Chow, D.H.K., 2010. Effects of Traction on Structural Properties of Degenerated Disc Using an In Vivo Rat-Tail Model. Spine 35, 1339-1345.

Lauterbur, P.C., 1989. Image formation by induced local interactions. Examples employing nuclear magnetic resonance. 1973. Clinical orthopaedics and related research, 3-6.

Lotz, J.C., 2004. Animal Models of Intervertebral Disc Degeneration: Lessons Learned. Spine 29, 2742-2750.

Luna, L.G., Armed Forces Institute of Pathology (U.S.), Armed Forces Institute of Pathology (U.S.). 1968. Manual of histologic staining methods of the Armed Forces Institute of Pathology, 3d ed. Blakiston Division, New York,.

Maclean, J.J., Lee, C.R., Alini, M., Iatridis, J.C., 2004. Anabolic and catabolic mRNA levels of the intervertebral disc vary with the magnitude and frequency of

in vivo dynamic compression. Journal of orthopaedic research : official publication of the Orthopaedic Research Society 22, 1193-1200.

MacLean, J.J., Lee, C.R., Grad, S., Ito, K., Alini, M., Iatridis, J.C., 2003. Effects of Immobilization and Dynamic Compression on Intervertebral Disc Cell Gene Expression In Vivo. Spine 28, 973-981.

MacLean, J.J., Roughley, P.J., Monsey, R.D., Alini, M., Iatridis, J.C., 2008. In vivo intervertebral disc remodeling: kinetics of mRNA expression in response to a single loading event. Journal of orthopaedic research : official publication of the Orthopaedic Research Society 26, 579-588.

Marjanska, M., Waks, M., Snyder, C.J., Vaughan, J.T., 2008. Multinuclear NMR investigation of probe construction materials at 9.4T. Magnetic Resonance in Medicine 59, 936-938.

Massengale, M., 2012. Distraction Techniques.

Masuda, K., Aota, Y., Muehleman, C., Imai, Y., Okuma, M., Thonar, E.J., Andersson, G.B., An, H.S., 2004. A Novel Rabbit Model of Mild, Reproducible Disc Degeneration by an Anulus Needle Puncture: Correlation Between the Degree of Disc Injury and Radiological and Histological Appearances of Disc Degeneration. Spine 30, 5-14.

Nerlich, A.G.M.D.P., Schleicher, E.D.P., Boos, N.M.D., 1997. 1997 Volvo Award Winner in Basic Science Studies: Immunohistologic Markers for Age-Related Changes of Human Lumbar Intervertebral Discs. Spine 22, 2781-2795.

Onel, D., Tuzlaci, M., Sari, H., Demir, K., 1989. Computed tomographic investigation of the effect of traction on lumbar disc herniations. Spine 14, 82-90.

Palepu, V., Kodigudla, M., Goel, V.K., 2012. Biomechanics of disc degeneration. Advances in orthopedics 2012, 726210.

Raj, P.P., 2008. Intervertebral disc: anatomy-physiology-pathophysiology-treatment. Pain practice : the official journal of World Institute of Pain 8, 18-44.

Ramos, G., Martin, W., 1994. Effects of vertebral axial decompression on intradiscal pressure. Journal of Neurosurgery 81, 350-353.

Roughley, P.J., 2004. Biology of intervertebral disc aging and degeneration: involvement of the extracellular matrix. Spine 29, 2691-2699.

Saunders, H.D., 1983. Use of spinal traction in the treatment of neck and back conditions. Clinical orthopaedics and related research, 31-38.

Schaumburg, H.H., Zotova, E., Raine, C.S., Tar, M., Arezzo, J., 2010. The rat caudal nerves: a model for experimental neuropathies. Journal of the peripheral nervous system : JPNS 15, 128-139.

Schizas, C., Kulik, G., Kosmopoulos, V., 2010. Disc degeneration: current surgical options. European cells & materials 20, 306-315.

Schnake, K.J., Putzier, M., Haas, N.P., Kandziora, F., 2006. Mechanical concepts for disc regeneration. European spine journal : official publication of the European Spine Society, the European Spinal Deformity Society, and the European Section of the Cervical Spine Research Society 15 Suppl 3, S354-360.

Setton, L.A., Chen, J., 2004. Cell mechanics and mechanobiology in the intervertebral disc. Spine 29, 2710-2723.

Sheehan, D.C., Hrapchak, B.B., 1987. Theory and practice of histotechnology, 2nd ed. Battelle Press : Distributed by Lipshaw, Columbus, Ohio : Detroit, Mich.

Showalter, B.L., Beckstein, J.C., Martin, J.T., Beattie, E.E., Espinoza Orias, A.A., Schaer, T.P., Vresilovic, E.J., Elliott, D.M., 2012. Comparison of animal discs used in disc research to human lumbar disc: torsion mechanics and collagen content. Spine 37, E900-907.

Stinnett-Donnelly, J.M., MacLean, J.J., Iatridis, J.C., 2007. A Removable Precision Device for In-Vivo Mechanical Compression of Rat Tail Intervertebral Discs. Journal of Medical Devices 1, 56.

Swezey, R.L., 1983. The modern thrust of manipulation and traction therapy. Seminars in arthritis and rheumatism 12, 322-331.

Thompson, J.P., Pearce, R.H., Schechter, M.T., Adams, M.E., Tsang, I.K., Bishop, P.B., 1990. Preliminary evaluation of a scheme for grading the gross morphology of the human intervertebral disc. Spine 15, 411-415.

Tubach, F., Beauté, J., Leclerc, A., 2004. Natural history and prognostic indicators of sciatica. Journal of Clinical Epidemiology 57, 174-179.

van der Heijden, G.J.M.G., Beurskens, A.J.H.M., Koes, B.W., Assendelft, W.J.J., de Vet, H.C.W., Bouter, L.M., 1995. The Efficacy of Traction for Back and Neck Pain: A Systematic, Blinded Review of Randomized Clinical Trial Methods. Phys Ther 75, 93-104.

Vo, N., Niedernhofer, L.J., Nasto, L.A., Jacobs, L., Robbins, P.D., Kang, J., Evans, C.H., 2013. An overview of underlying causes and animal models for the study of age-related degenerative disorders of the spine and synovial joints. Journal of orthopaedic research : official publication of the Orthopaedic Research Society 31, 831-837.

Walsh, A.J.L., Lotz, J.C., 2004. Biological response of the intervertebral disc to dynamic loading. Journal of Biomechanics 37, 329-337.

Walter, B.A., Korecki, C.L., Purmessur, D., Roughley, P.J., Michalek, A.J., Iatridis, J.C., 2011. Complex loading affects intervertebral disc mechanics and biology. Osteoarthritis and cartilage / OARS, Osteoarthritis Research Society 19, 1011-1018.

Watson, P.J., Main, C.J., Waddell, G., Gales, T.F., Purcell-Jones, G., 1998. Medically certified work loss, recurrence and costs of wage compensation for back pain: a follow-up study of the working population of Jersey. Rheumatology 37, 82-86.

Wilke, H., Neef, P., Hinz, B., Seidel, H., Claes, L., 2001. Intradiscal pressure together with anthropometric data--a data set for the validation of models. Clinical biomechanics (Bristol, Avon) 16 Suppl 1, S111-126.

Wuertz, K., Godburn, K., MacLean, J.J., Barbir, A., Donnelly, J.S., Roughley, P.J., Alini, M., Iatridis, J.C., 2009. In vivo remodeling of intervertebral discs in response to short- and long-term dynamic compression. Journal of orthopaedic research : official publication of the Orthopaedic Research Society 27, 1235-1242.

Wynne-Davies, R., 1975. Congenital vertebral anomalies: aetiology and relationship to spina bifida cystica. Journal of medical genetics 12, 280-288.

Yurube, T., Nishida, K., Suzuki, T., Kaneyama, S., Zhang, Z., Kakutani, K., Maeno, K., Takada, T., Fujii, M., Kurosaka, M., Doita, M., 2010. Matrix metalloproteinase (MMP)-3 gene up-regulation in a rat tail compression loading-induced disc degeneration model. Journal of orthopaedic research : official publication of the Orthopaedic Research Society 28, 1026-1032.

Zhao, C.Q., Wang, L.M., Jiang, L.S., Dai, L.Y., 2007. The cell biology of intervertebral disc aging and degeneration. Ageing research reviews 6, 247-261.